Glacier Classification and Movement Estimation using SAR Polarimetric and Interferometric Techniques

SAHIL SOOD

ITC SUPERVISOR Prof. Dr. Ir. A. Stein

IIRS SUPERVISOR Dr. Praveen Thakur

Glacier Classification and Movement Estimation using SAR Polarimetric and Interferometric Techniques

SAHIL SOOD
Enschede, The Netherlands

Thesis submitted to the Faculty of Geo-information Science and Earth Observation of the University of Twente in partial fulfilment of the requirements for the degree of Master of Science in Geo-information Science and Earth Observation.

Specialization: Geoinformatics

FACULTY OF GEO-INFORMATION
SCIENCE AND EARTH OBSERVATION,
UNIVERSITY OF TWENTE,
ENSCHEDE, THE NETHERLANDS

INDIAN INSTITUTE OF REMOTE SENSING
Indian Space Research Organisation
Department of Space, Government of India

DISCLAIMER

Dedicated to my mother and father!

ABSTRACT

Glaciers are directly affected by the recent trends of global warming. Himalayan glaciers are located near Tropic of Cancer this belt receives more heat thus Himalayan glaciers are more sensitive to climate change. Major rivers of Asia originates from these glaciers and they are only source of fresh water for millions of people living in Indian sub-continent. Due to highly rugged terrain and inaccessibility of certain areas satellite obtained information is used to monitor glaciers. Mapping of accumulation and ablation areas and determining the rate of flow of the ice are important factors which determine its rate of melt of a glacier. Samudra Tapu glacier, used in this study, located in the Great Himalayan range of north-west Himalaya. This study focusses on the classification of the glacier and estimating its movement. Different glacier facies were mapped using multi-temporal SAR datasets and polarimetric decompositions. Support Vector Machines (SVMs) were used for final classification. Equilibrium Line Altitude (ELA) which divides the accumulation and ablation regions was determined at 5200 m. More than 50% of the total area is found as accumulation, since Samudra Tapu glacier from a cirque at high altitudes. Glacier flow was estimated using Interferometric Synthetic Aperture Radar (InSAR) using ascending pass ERS-1/2 datasets. High value of coherence of SAR return signal was obtained from these datasets with one day temporal difference. A maximum velocity of 57 cm/day in the month of May was found in the northern branch at high accumulation area. Spatial analysis of velocity patterns with respect to slope and aspect show that high rates of flow was fond in southern slopes and movement rates generally increase with increase in slope. Seasonal glacier flow and long term glacier monitoring was estimated for the ablation area of the glacier using offset feature tracking. Images pairs representing different seasons and time periods were used in this technique. A mean displacement of 13.1 cm/day in azimuth direction and 8.9 cm/day was estimated during the months of September and October 2013. Variation in glacier flow was noticed between different times periods this clearly suggests that glacier flow varies with season.

Keywords

Climate change, Himalayan glacier, Accumulation, Ablation, Cirque, SVMs, ELA, Glacier flow, InSAR, Feature tracking,

ACKNOWLADGEMENTS

Attitude determines altitude

I want to thank all my teacher form Indian Institute of Remote Sensing (IIRS) and ITC - Faculty of Geoinformation Science and Earth Observation for giving me knowledge, concepts, recources and technically supporting me and guiding me.

I want to show my sincere acknowledgement towards my supervisor Dr. Praveen Thakur for providing me all the data required for the successful completion of this research. I want to thank him in helping me to understand the advanced concepts of SAR interferometry; his expertise in Himalayan glaciers and his guidance helped me a lot.

I thank Prof. Dr. Alfred Stein for his guidance, support and motivation throughout my research phase. I have been privileged to have a supervisor like him. His deep understanding in spatial statistics and his frequent e-mail replies and his willingness to help his students are worth parsing.

I respect Dr. Valentyn Tolpekin for his kind and helpful nature. I thank him for his help in teaching the basic concepts in SAR interferometry and polarimetry.

A special note of gratitude to Dr. Y. V. N. Krishna Murthy (Director, IIRS). I also thank Dr. S K Srivastav, Head of Department, Department of Geoinformatics for his valuable advices and concern which have really helped me during my research. I also thank Mr. P L N Raju, Group Head, Remote Sensing and Geoinformatics group for his valuable advices and providing me necessary resources to complete my project.

I want to thank research fellows Mr. Ankur Dixit and Mr. Arun for their help and motivation.

Mr. Prashant Chauhan Negi, a friend who came along with us during the field visit and clicked all the photographs.

At last but not least I would like to thank all my friends at IIRS for encouraging me and their timely help and support.

Sahil Sood

TABLE OF CONTENTS

LIST OF FIGURES

LIST OF TABLES

1 INTRODUCTION

1.1 Background

Glacier is a vast body of ice originated mainly from snowfall during many ages. A glacier is moving where the speed of movement and the spatial variation of downslope movement are largely determined by its weight. Glaciers are found in Polar Regions and in high mountain ranges all over the world(Funk, 2013). They are the source of fresh water for drinking, industry, irrigation and hydroelectric power generation(WWF, 2005). Glaciers are sensitive indicators of climate change that means even a small change in climate can lead to a rapid melting. In recent years due to global warming, these massive bodies of ice are reported to be melting at a much faster rate. This excessive melt water can lead to glacial lake outburst flood (GLOF), flash floods and avalanches in mountainous areas, sea level rise which causes threat to coastal communities(Eriksson et al., n.d.). Furthermore snow acts as a reflector to the incoming solar radiations as the snow cover is decreasing more radiations are absorbed by the earth this will in turn heat up the atmosphere and thus lead to rapid melting of ice caps and glacier(Muller, 2011). This necessitates the accurate and updated information of this ice mass.

Ice mass is directly affected by the accumulation and ablation of snow and ice (Frenierre et al., 2009). Glacier snow cover i.e. the snow pack on the top of the glacier, differs in the moisture content; because of variation in temperature at different altitudes. Higher reaches mainly consist of compressed form of snow, dry snow consequence of no or little melting even in summers. Moving downslope there is transition in the snowpack conditions, as it changes to firn, the wet snow which has survived the entire summer without being transformed to ice these are the building blocks of glacier (Paterson, 2000). At the lowest point seasonal snow is found covering debris and ice facies near the snout of the glacier. Type of snow pack determines the accumulation and ablation zones of a glacier. The accumulation zone is the zone where melting and refreezing of ice throughout the year occurs. The ablation zone is the zone near the snout of the glacier where the melting takes place in summers caused by even a small rise in temperature (Huang et al., 2011). Areas of dry snow and firn determine the accumulation zone of the glacier, and the debris covered ice facies are found in the ablation zone. Increase in accumulation results in ice mass thickening that in turn result into the lengthening of a glacier whereas increase in ablation leads to recession and melting of glacier (Hagen et al., 2004). Sum of accumulation and ablation per unit time is the net mass balance for a glacier. The Equilibrium Line Altitude (ELA) is the altitude that represents the transition from the accumulation zone to the ablation zone of the glacier (Huang et al., 2011) Glacial ice is not static; it moves under the effect of gravity determined by its weight. Therefore the density of the prevalent snow pack conditions has a direct impact on the movement of the glacier. Also as ice moves further down the valley there is transition in its state; it changes from dry snow to firn then into wet snow in the ablation area where it finally melts. Velocity estimates can predict the rate of transition of ice, which determine the accumulation and ablation areas. High velocity values have been observed in the accumulation zone. Hence if ice flows across the ELA and enters the ablation zone, melting leads to a negative mass balance. This means that the glacier is receding. These effects are more pronounced in the summer season than in the winter season (Kumar et al., 2011). Different rates of melt have been reported in the glaciers, so there is a need to study how the nature of ice mass, slope of the bed rock at different altitudes affect the movement of the glacier that leads to its melt(UNEP, 2009).

1.2 Motivation and Problem Statement

After the 'Little Ice Age' (1550-1850 AD) and recent trends in global warming show that glacier cover all over the world is decreasing(WWF, 2005). This research is focused on the Hindukush Himalaya which spreads from Jammu and Kashmir in the north-west to Arunachal Pradesh in the north-east. Himalayas are known as the water towers of Asia providing water to 1.5 billion people living in the downstream(Messerli et al., 2004; UNEP, 2009). But very less knowledge of this heavy glaciated area is present, further more due to high altitude, rugged and inaccessible terrain it is difficult to carry field study(Frey et al., 2012). Remote sensing can be used as an alternative approach to monitor these ice masses, as it can gather information without actual physical contact. However optical remote sensing has its limitations as these mountain glaciers are often under cloud cover, also the shadows of high mountains makes it difficult to separate glaciated and non-glaciated areas. Furthermore the optical properties of snow and ice are similar so it is difficult to discriminate between them(Gupta et al., 2005). But higher wavelength of the microwave region can be used to monitor glaciers because of cloud penetration capabilities and day and night coverage in case of active microwave sensors(Huang et al., 2011). Synthetic Aperture Radar (SAR) provides high resolution microwave data by the use of a large synthetic antenna. Furthermore the radar backscatter is influenced by physical properties of the material like surface roughness, dielectric constant and volume inhomogeneities thus can be used to discriminate between different types of scatters(Bindschadler, Jezek, & Crawford, 1987).

By classifying the snowpack of glacier as dry snow, firn and glacial ice we can identify the spatial extent of accumulation zone and the area where ablation takes place. These in turn define wet snow line i.e. altitude separating dry firn from wet snow, the ELA and snow line i.e. the lowest altitude where wet snow is present at the end of ablation season (Huang et al., 2011). The ELA is affected by the yearly precipitation and the melting of the snow but the wet snow line is not much affected by these yearly variations, but a permanent shift in the ELA will have an effect on the wet snow line which in turn will have an pronounced effect on the mass balance of the glacier(Konig et al., 2000). Different types of scattering mechanisms are observed in the glacier as microwave radiations are sensitive to the moisture content in the snow pack, radiations for higher frequencies are transparent to dry snow and volume scattering takes place where as for wet snow and glacier ice due to higher moisture content scattering takes place at the surface(Rott et al., 1987). Using both co polarized and cross polarized SAR channels i.e. fully polarimetric SAR datasets highly descriptive results are obtained and can give enhanced classification results(Shimoni et al., 2009). For the purpose of classification machine learning algorithms, Support Vector Machines (SVMs) results in higher level of accuracy in comparison to statistical approaches like Maximum Likelihood (ML) and Artificial Neural Networks (ANN) with less number of training samples and are computationally fast(Tso et al., 2009)

The backscatter signal in SAR channel consists of amplitude and the phase information; phase is the fraction of the wave length that has elapsed relative to the origin. The phase of a single SAR image is of no use but the phase difference between two SAR acquisitions can provide the topographic information as well as the surface deformations this process is called interferometry(Pellika et al., 2009). Interferometric SAR (InSAR) has a precision of few millimeters, but highly dependent on the phase coherence between two acquisitions and also the displacement values are not calculated in plane orthogonal to the radar Line Of Sight (LOS)(Gourmelen et al., 2011). InSAR can be used to estimate the surface displacements of glaciers but as these ice masses are fast moving the temporal difference in the images should be less to retain high degree of coherence; European Space Agency ERS1/2 TANDEM mission provides C-band SAR data with one day temporal resolution which can be used for accurate velocity estimates, but these datasets had constraints of limited number of scenes at a certain time period. An alternative approach is feature tracking which uses high resolution coregistered SAR or optical satellite images and by using cross correlation techniques detects identifiable features like crevasses and determines the rate of flow of glaciers(Giles et al., 2009). The slope and aspect parameters are the derivatives of topography of the bed rock; these have a direct effect on the movement of the glacier and can be spatially analyzed.

1.3 Research Identification

The spatial extent of the accumulation and ablation zone determines ELA which affects the mass balance of the glacier. Different rates of melts have been observed in glaciers even in same spatial domain. The rate of melt is highly affected by the rate of flow of the glacier i.e. how fast the ice flows and enters the ablation zone where it melts and also the extent of accumulation and ablation regions. The velocity of ice flow depends on the bed rock topography and also the aspect, as the south aspect is more exposed to sunlight so high rate of melt is noticed leading to a higher rate of flow in southern aspects. So there is need to study all these factors for the monitoring of the glaciers.

1.3.1 Research Objectives

- To classify glaciers on the basis of the snow pack at different elevations using backscatter characteristics and polarimetric decompositions.
- To estimate the glacier displacement using SAR interferometry and feature tracking.

1.3.2 Sub – Objectives

- To determine the altitude of wet snow line, equilibrium line and snow line.
- To carry out spatial analysis of the terrain parameters on the movement of the glacier.
- To Estimate the rate of flow for different classified zones.

1.4 Research Questions

- How useful is Polarimetric SAR (PolSAR) for identifying different glacier facies?
- How to map the accumulation and ablation areas for a glacier?
- What is the analysis of accuracy, robustness and efficiency of SVM in comparison to other classification methods?
- How can Interferometric SAR (InSAR) be used to estimate the glacier displacement?
- What is the accuracy of the estimated glacier displacement obtained from InSAR and offset feature tracking of SAR and optical datasets?
- What are the effects of terrain parameters and climatic conditions on the movement of the glacier?

1.5 Innovation Aimed At

The innovation of this research is aimed at studying that how prevalent snow pack conditions at different altitudes affects the movement of glacier this type of work has not be done in the Indian Himalayas.

1.6 Related Work

Research related to identifying the different zones of the glacier and estimation of the velocity of the glacier using SAR interferometry and feature tracking on high resolution SAR and optical data has been done in the following papers.

- Patrington, (1998) used multitemporal ERS-1 SAR datasets to identify the different glacier facies in Greenland ice sheet and Warangell St. Elias Mountain Alaska.
- Rott et al., (1987) studied the angular and spectral behavior of radar backscattering on various snow types in Swiss Alps.
- Huang et al., (2011) used fully polarimetric ALOS/PALSAR for the purpose of glacier classification and snow line detection in Dongkemadi glacier in Qinghai-Tibetan plateau. Support Vector Machines (SVMs) are used to classify the selected features.
- Kumar et al., (2011) used one day temporal difference ascending and descending pass ERS 1/2 tandem mission data to estimate the 3-D velocity of Siachen glacier in Himalayas.
- Li et al., (2008) studied Nabesna glacier one of the largest land terminus glacier in North America. Interferometric techniques were used to estimate the velocity using ERS 1/2 SAR datasets.
- Bhattacharya et al., (2012) studied land surface displacement due to unplanned mining using Differential Interferometry (DInSAR) in Jharia coal fields at millimeter accuracy.
- Zongli et al., (2012) used SAR feature tracking on L-band ALOS/PALSAR datasets to obtain surface velocity of Yengisogat glacier in Karakoram Mountains.

1.7 Thesis Structure

This thesis is divided into seven chapters. The *first chapter* gives an introduction of the research, objectives and the sub-objectives that need to be achieved. The *second chapter* presents the information about the related work that has already been done in the field of glaciers and techniques that are used in this study. The proposed methodology has been discussed in the *third chapter*. *Fourth chapter* discuses about the study area considered for this research the reasons for selecting it, various software and datasets used. The various results obtained and their analysis is done in the *fifth chapter*. The *sixth chapter* discusses the various results obtained using the proposed methodology. The *seventh chapter* concludes the research, answers all the research questions and also gives scope for improvements in current research outcomes.

2. LITERATURE REVIEW

2.1 Glacier

Glacier is formed where the accumulation exceed ablation, in summers the snow will undergo metamorphism and changes into ice which deforms and move downwards under its own weight. This ice mass continues to flow downhill until it reaches a point in the lower altitude where the entire ice supplied from the higher altitudes is melted(Pellika et al., 2009). Over the past earth's surface has experienced large periods of glaciations separated by warm periods. During the peak of glaciations 47 million km^2 of area was covered with glaciers which is about three times the present ice cover. Cause of these glaciations is due to the variation of earth's orbit around the sun causing 10% change in the incoming solar radiations reaching the earth's surface(Kulkarni, 2007). In present scenario glaciers, ice caps and continental ice sheets cover upto 10% of earth's land surface which is about 15,000,000 km^2(Raina, 2005). They are found all over the world, most of them lie in poles and all the continents of the world except Australia, covering three quarter of world fresh water resources(UNEP, 2009). Glaciers are unique source of fresh water for irrigation, drinking and hydroelectric power generation. They are also the source of tourism for people living in the mountain areas(Jo et al., 1998).

Glacier are sensitive to climatic variations because of their proximity to melt therefore are considered as indicators of climate change. In recent years global warming has accelerated due to increase in the concentration of greenhouse gasses leading to a rise of temperature by about 0.18-0.35°C per decade, this increasing temperature affects the glaciers both in terms of length and volume(Jaenicke et al., 2006). Mass balance is the indicator of the health of the glacier; it is the difference between accumulation and net ablation. A positive value indicates that there in increase in the length and volume of ice of the glacier whereas negative value shows that glacier is depleting(Bolch et al., 2011). Changes in atmospheric conditions such as solar radiation, air temperature, precipitation and cloudiness determine whether the precipitation falls as snow or rain is a critical factor that affects the mass balance of the glacier(Zemp et al.). These changes in the mass balance causes change in the volume and thickness which in turn affects the flow of the glacier leading to surges i.e. substantial glacier advance much higher than the normal flow. A thick layer of debris also affects the rate of ablation of ice(Tiwari et al., 2012). Temperate glaciers are not under the influence of thick debris cover, surges or calving and are best to study the effect of climate change on glacier(UNEP). Determination of glacier facies is important for snow melt runoff calculations and for accessing carbon dioxide derived changes on the climate(Patrington, 1998). Glacier motion studies help us to study the changes in mass fluxes and response to climate change. Knowledge of glacier flow gives us better understanding of the formation of glacial lakes and the associated hazards. Also glacier velocities are also input to various numerical glacier model(Heid et al., 2012).

Glacier monitoring was initiated in 1894 in Zurich Switzerland the data derived from field measurements and remote sensing provide a fundamental basis for study of glacier changes in time and space(WGMS, UNEP).

2.2 Himalayan Glaciers Overview

Himalaya is youngest mountains in the world and around 17% of its area i.e. 33,000 sq. km is covered by glaciers(Pandey et al., 2012). Himalayan glaciers are located near Tropic of Cancer they spread from latitude 36°N to 27°N and longitude 72°E to 96°E. This belt receives more heat than Arctic, Antarctic and Temperate regions of the world so the glaciers located in this region are more sensitive towards climate change(Ahmad et al., 2004). Ten of the largest Asian rivers originate from the Himalayas providing water to 1.3 billion people living in this sub-continent. This snow covered area is not only the source of fresh water but also influences the monsoon rainfall in the region(Khadka et al., 2014).

Recent trends of global warming are affecting the Himalayan glaciers. Global circulation climate model predicts that continental interior of Asia i.e. Himalayas shows greater level of climate change due to human induced global warming(Haughton et al., 2001). These changes in climate significantly influence the glacial retreat, every glacier responds to the change in climate differently depending on the size, area, altitude, orientation and moraine cover(Kulkarni, 2007). The distribution and style of glaciations in Himalayas are influenced by South-West Indian monsoon, the mid latitude western disturbances and El Nino Southern Oscillations (ENSO)(Owen et al., 1998).A 20% decrease in the summer runoff has been reported in Hunza and Shyock rivers in Karakoram. This can be linked to 1°C fall in mean summer temperatures since 1961 also expansion and thickening is reported in glaciers lying in the Karakoram region whereas towards the eastern side retreat of glaciers at substantial rates is reported so the glaciers are showing contrast from western to eastern Himalaya(Pandey et al., 2012). The glaciations are asynchronous in the different parts of Himalayas and also with global glaciations, the coupling between the regional climate and global climate can yield valuable information that how climate system affects glaciations(Owen et al., 2002). In Himalayas the glaciation depends on the regional climate and the variations in the global climate which have greater impact in this region. The variation in glaciations in Himalayan region is due to the altitude, terrain and orientation of the area so these morphometric factors should be studied to have a better understanding of glaciations in this region.

Changes in the length, areal extent, mass balance and the snow line altitude at the end of ablation season are the impacts of climate change(Berthier et al., 2007). But due to inhospitable climatic conditions and high altitude of these glaciers very little databases are available. As the glaciations are different in different regions in Himalayas the nature of the glaciers and their response to the changing climate is also different, from south west to north east there is an increase in the mean glacier elevation by about 1500 m and decrease in the relative debris cover from 22% to 6% due to different climatic and topographic conditions(Frey et al., 2012). This debris cover plays an important role by slowing down the rate of melt of the glacier by insulation the glacier ice from the incoming solar radiations. Furthermore more ice volumes are located in the ablation areas because of the gentle slopes.

2.3 Glacier Study Using Remote Sensing

Due to large spatial coverage high temporal and spatial resolution, repetitive coverage and cost effectiveness of satellite data in comparison to filed visit remote sensing has provided an alternative approach for glacial studies(Gao et al., 2001). World Glacier Monitoring Service (WGMS) and Global Land-Ice Measurements from Space (GLIMS) are some of the renowned organizations which have taken initiative to make glacial inventory using field visits and remote sensing techniques(Kargel et al., 2005;Aizen et al., 2007).

Remote sensing has provided an important tool for monitoring changes in Equilibrium Line Altitude (ELA), changes in the annual mass balance, advance and retreat of glaciers, changes in the aerial extent of glaciers and formation of supraglacial lakes(Frey et al., 2012;Wagnon et al., 2007;Berthier et al., 2007;Kulkarni et al., 2007). All these studies were carried out using high resolution multispectral optical satellite imagery but they have limitations of working under cloudy conditions. This constraint can be countered by using higher wavelengths of microwave region which can penetrate clouds. SAR sensor can also penetrate dry snow due to low moisture content and can provide information about the features under snow cover like crevasses and moraines(Rott et al., 1987). SAR coherence images are used for glacier identification for debris covered glaciers(Frey et al., 2012). Konig et al. (2000) used multi polarization SAR for equilibrium and firn line detection these are important factors in determining the mass balance.

Glacier velocity can be determined accurately by frequent filed visits over the same area but lack spatial coverage in the inaccessible parts of the glacier(Scherler et al., 2008). Using SAR interferometric techniques it is possible to estimate the glacier velocities in images with a high degree of coherence. Kumar et al., (2011) used ERS1/2 ascending and descending tandem datasets to estimate the velocity of Siachen glacier in Karakoram Mountains, high rate of flow 43cm/day has been identified in the accumulation area of the glacier. A German satellite TanDEM-X has the goal of generating a global Digital Elevation Model (DEM) with high vertical accuracy of 2-4 m using X band SAR interferometry which will be highly useful in glacial studies(Floricioiu, 2011). An alternative approach for estimating glacier surface velocity is offset tracking this technique is not limited by temporal decorelation between the two SAR datasets and uses high resolution coregistered optical and SAR images to track identifiable features like crevasses and determine the velocity of the glacier(Strozzi, et al., 2002).

2.4 Physics of Glaciers and Microwave Response

2.4.1 Type of Snow Pack(Paterson, 2000)

1. Snow: - It is precipitation in from of crystals formed by the freezing of water vapors and has a low density of about 50-70 Kg/m^3
2. Firn: - It is the intermediate stage of wetted snow that has survived the entire summer without being transformed into ice, it is found in the region where very less melting takes place. Being the intermediate stage it is denser than snow with density of about 400-830 kg/m^3
3. Ice: - When the interconnecting air passages in firn are sealed off it becomes highly dense about 830-917 kg/m3, air is present in the form of bubbles and density increases with further compression of these air bubbles.

2.4.2 Radar Backscatter in Different Snow Pack

The snow cover of glacier i.e. snow pack is not homogeneous it changes with varying altitude. As we move down slope there is rise in temperature which leads to increase in the liquid water content. This changes the dielectric constant of the prevalent snow pack conditions. The electrical properties of the material i.e. the moisture content, surface roughness and volume inhomogeneities of the scatters, also the wavelength polarization and incidence angle at the transmitting end affect the radar backscatter signals(Bindschadler et al., 1987). The angular and spectral behavior of back scattering is used to differentiate the different type of scatters (Rott et al., 1987). Snow is transparent to microwave radiations; C- band can penetrate up to tens of m in dry snow. Penetration is highly dependent on the liquid water content of the snow pack and the wavelength of the SAR signals, more penetration is noticed for L-band due to higher wavelength. In dry snow scattering will occur mostly at the internal layers due to volume in homogeneities and less at the surface(Rott et al., 1987). In case of wet snow and glacial ice scattering will take place at the surface as black body properties are approached when surface is wet i.e. high emission and low backscattering. But glacial ice comparatively rough as compared to wet snow giving higher scattering returns in comparison to specular reflection for wet snow facies. Also microwave penetration increases during night due to refreezing of the snow pack. Even if damp snow is under refrozen fresh or dry snow the backscatter values will show very less difference as the backscatter comes from damp snow because of penetration(Patrington, 1998). The intensity of backscatter increases in lower areas of firn having a similar backscatter to rough glacial ice it is due to the increase in surface roughness of snow at lower altitudes(Rott et al., 1987). Accurate modelling of the scattering behavior is difficult as surface roughness is comparable to the magnitude of the wavelength there is increase in the amount of scattering with the decrease in the wavelength(Rott et al., 1987).

2.4.3 Different Zones of the Glacier and their Scattering Mechanism

Glacier facies are distinct zones on the surface of glacier and form accumulation and ablation areas.

Dry Snow Zone

This zone is found at the top elevation in the glaciers where the mean annual temperature is about -25°C, because of the low temperature no melting takes place even in summers. Dry snow is the mixture of air and snow and compacted under its own weight. In this zone volume scattering is dominant and any variation in the backscatter values is due to the difference in the snow grain size. This zone is found only in the glaciers in Antarctica, Greenland, some glaciers in Alaska and Svalbard at high elevations. The boundary between this zone and next is called dry snow line(Patrington, 1998;Konig et al., 2001).

Percolation Zone

Surface melting occurs in this zone and water percolates a certain distance into snow where it refreezes leading to the formation of ice lenses and pipe like structures called ice glands. The freezing of melt water releases latent heat of condensation causing further warming of snow. A high value of backscatter in winter months is due to these ice lenses, there is a drop in backscatter values in the melt season as the surface becomes wet. As we move down the glacier we reach a point where all the snow deposited from the end of previous summer has melted this point is called wet snow line(Konig et al., 2001).

Wet Snow Zone

Further down the percolation zone entire accumulation of snow has melted and then refreeze leading to a larger crystal size i.e. transformation of snow to ice. The scattering mechanism changes from volume scattering in percolation zone to surface scattering in wet snow zone and there is a striking difference in the backscatter values. This zone has low backscatter values in spring and summer due to melt conditions. The lower part of wet snow consists of slush, where melting is rigorous and appear as damp areas in the SAR images(Patrington, 1998).

Superimposed Ice Zone

At lower elevations, huge amount of melt water is produced so that the ice layers merge into a continuous mass this is called superimposed ice. These zones are also found in the wet snow zone buried beneath the firn. The boundary between wet snow zone and superimposed ice is called snow line or firn line and is determined at the end of the ablation season. Superimposed ice zones are very difficult distinguish from bare ice zones as both are made up of ice but there is a higher degree of smoothness in superimposed ice zone relative to bare ice this can be used as a discriminating factor between the two facies. The lower boundary of the superimposed ice is taken as equilibrium line, and is important in mass balance studies.(Patrington, 1998;Paterson, 2000).

Ablation Area

Lowest part of glacier consists of bare ice; here the total accumulation is lost to melting. In winter season these ice facies are covered with dry snow, less backscatter is observed due to attenuation by dry snow. As snow melts backscatter decrease due to the presence of melt water content. At the end of ablation season when all the seasonal snow has melted higher backscatter returns are observed from the rough bare ice surfaces(Patrington, 1998).

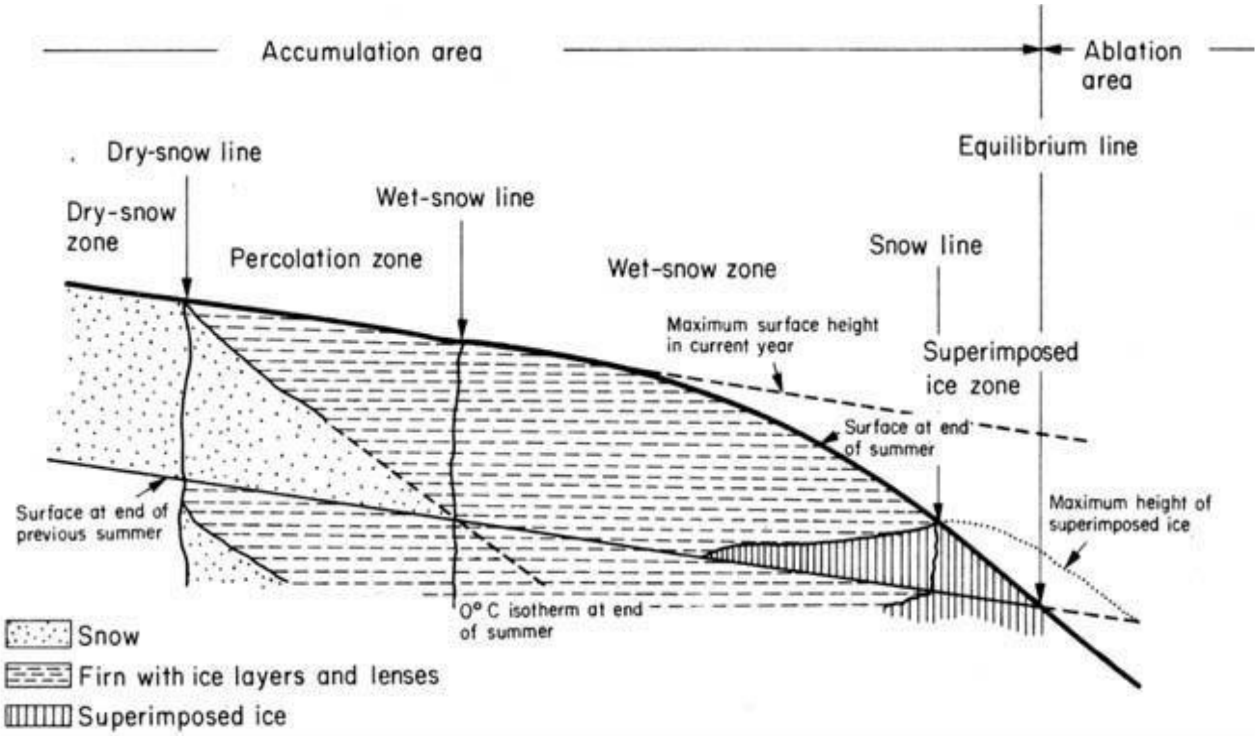

Figure 1: Cross-sectional structure of glacier (Paterson, 2000)

2.4.4 Glacier Flow

The flow characteristics of glaciers determine that how it will react to the climate change. Glacier velocity is maximum in the central part and decreases along the sides. Ice moves slowest near the snout and ice at the surface moves more rapidly than ice at depth. The velocity vectors are not parallel to the surface but are inclined downwards towards the surface bed in the accumulation area and upwards in the ablation area(Paterson, 2000).

Conditions for internal deformation in glacier flow are: -

a) If ice is warm and sets on the bed rock basal sliding occurs. (Figure_2A)
b) Deformation when bed rock is frozen. (Figure_2B)
c) Ice deformation can occur when ice is warm and unconsolidated, basal sliding contributes towards ice flow(Siegert, 2008). (Figure_2C)

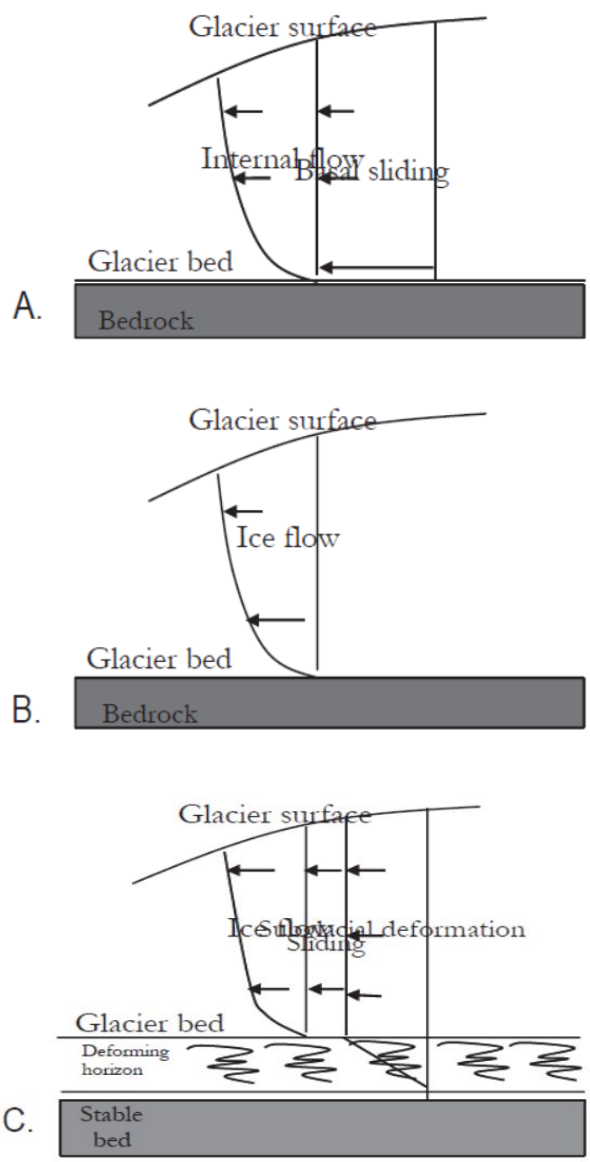

Figure 2: Flow controlling process (Siegert, 2008)

2.5 Support Vector Machines (SVMs)

The conventional statistical classification algorithms like maximum likelihood uses empirical sense based on previous knowledge to minimize the classification error which is related to the distribution of the training samples. SVMs are machine learning algorithms and uses the concept of minimizing the probability of misclassifying data point drawn randomly from a probability distribution that means SVM finds a global minimum for misclassifying a data point(Tso et al. 2009). SVM constructs a hyper plane which is decision boundary on the basis of the properties of training samples. The margin of separation between sample data points and the separating hyperplane should be maximum. All training samples are not used to construct the hyperplane but only the points near the hyperplane are used these points are called support vectors(Tso et al., 2009).

Linear Classification

Separable case: - Assume there are two linearly separable classes and training datasets represented as $\{x_i, y_i\}$, $i = 1 \ldots n$, $y_i \epsilon$ $\{1,-1\}$ and x_i are observed multispectral features and y_i is the label information for class. The support vector machine builds an optimal hyperplane in such a way that the distance from the hyperplane to the support vectors is maximum this distance is called margin(Tso et al., 2009)

The hyperplane is represented as:

$$W^T x + b = 0 \tag{1}$$

Here x is the point on hyperplane; W is normal to the hyperplane; T denotes matrix transposition and b is the bias. The distance from the hyperplane to the origin is $|b|/\|W\|$. Now all the training datasets should satisfy the following constraint(Tso et al., 2009):

$$W^T x_i + b \geq +1 \textit{ for } y_i = +1 \tag{2}$$

$$W^T x_i + b \leq -1 \text{ for } y_i = -1 \tag{3}$$

The two equations can be combined as follows:

$$y_i \left(W^T x_i + b\right) -1 \geq 0 \tag{4}$$

We can generate two hyperplane representing each class with distance $|1 - b|/\|W\|$ and $|-1 - b|/\|W\|$. The support vectors of both classes lie on their respective hyperplane such that the value of margin is $2/\|W\|$. For optimal class separation we have to maximize the value of margin(Tso et al., 2009).

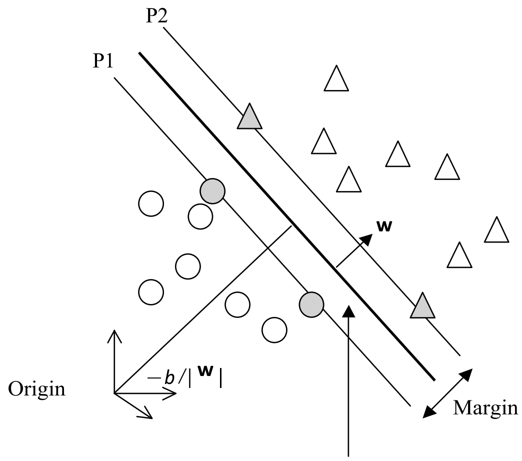

Optimal separating hyperplane: $w^T x + b = 0$

Figure 3: SVM for linear separable case(Tso et al., 2009)

The non-separable case: - If the information classes are not separated by linear boundaries slack variables are introduced to relax the constraints in the formation of the hyperplane. When slack variables are included the equation becomes(Tso et al., 2009):

$$y_i(W^T x_i + b) \ -1 \geq \ 1 - \ \xi_i \qquad (5)$$

These slack variables allow the inclusion of training samples located on the other side of the hyperplane larger the value of the hyperplane less is the generalization.

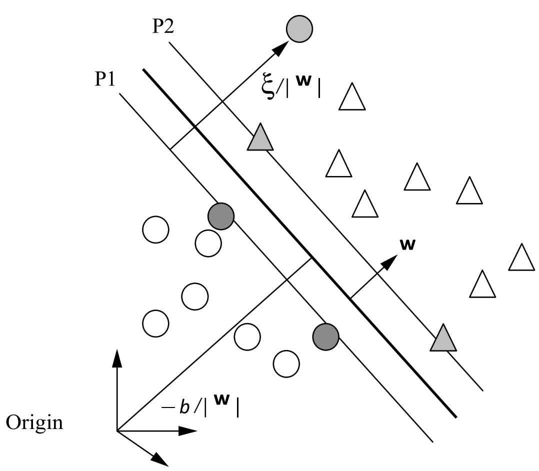

Figure 4: SVM for partially separable case(Tso et al., 2009)

Nonlinear Classification

In some cases a linear hyperplane is not able to separate the classes in such cases we have to map the classes into a higher dimension space to improve the class separability. Various kernel functions are used for the mapping of the training samples into higher dimensional space so that the training samples are spread so that the fitting of a linear hyperplane is facilitated. Some commonly used kernel functions are polynomial function, radial basis function, Gaussian radial basis function and sigmoid function. The performance of SVM is related to the choice of the kernel function used once the kernel function is determined the related parameters are chosen(Tso et al., 2009).

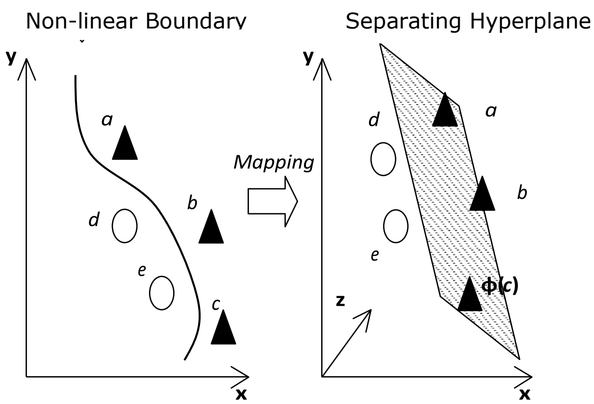

Figure 5: Non-linear SVM mapped to higher dimensional space(Tso et al., 2009)

2.6 SAR Interferometry

Glacier flow is directly related to its melt because the flow of ice into the ablation area determines how fast it will melt, so it is critical factor to study the effect of global warming on glaciers. SAR interferometric technique is used for detecting and monitoring centimeter scale deformations on earth's surface(Reigber et al., 2003). SAR signal carries the information of radar backscattered intensity and phase. The complex SAR images are acquired from slightly different locations in space ranging from few meters to few hundred meters this distance is called baseline. The value of phase depend on the radar wavelength and roundtrip path length between the SAR and target on the ground(Kumar et al., 2011). InSAR uses the phase information from two SAR images having same wavelength and covering same area, by aligning the two SAR images pixel by pixel phase difference is calculated(Li et al., 2008).

The interferometric phase difference between two SAR images taken at different points is represented by the equation(6)(Reigber et al., 2003)

$$\phi = \phi_{topo} + \phi_{earth} + \phi_n + \phi_{atm} + \phi_{\Delta r} \tag{6}$$

where ϕ_{topo} denotes the phase difference contribution caused by terrain topography, ϕ_{earth} systematic phase component corresponding to flat earth, ϕ_n is the noise contribution due to limited signal to noise ratio (SNR) and temporal decorelation effects, ϕ_{atm} phase contribution due to different atmospheric conditions, $\phi_{\Delta r}$ differential phase related to changes in slant range distance. The ideal condition to monitor surface deformations occurs when the baseline between two acquired images is zero(Bhattacharya et al., 2012). For non-zero baseline the phase shift is due to ground movement and topographic effects. The topographic component can be removed by using an external digital elevation model (DEM), a stimulated interferogram or by using an interferogram generated from a common master image(Kumar et al., 2011). This approach is called Differential Interferometric SAR (DInSAR) removes the effect of ϕ_{topo} and ϕ_{earth} from the interferometric phase.

Coregistration of images is done with subpixel accuracy so that the phase difference is calculated from the same corresponding pixel from both the SAR images. The mean square error is given by the equation(7)(Brown, 1992).

$$D(m,n) = \sum_i \sum_j [F_1\,(j,k) - F_2\,(j-m,k-n)]^2 \tag{7}$$

Where m and n are offset values in range and azimuth. $F_1(i,j)$ and $F_2(i,j)$ are master and slave images the equation can be expanded as

$$D(m,n) = [F_1\,(j,k)]^2 - 2 \times [F_1\,(j,k)] \times [F_2\,(j-m,k-n)] + [F_2\,(j-m,k-n)]^2 \tag{8}$$

The terms $[F_1\,(j,k)]^2$ and $[F_2\,(j-m,k-n)]^2$ in the above equation is the image energy.

$2 \times [F_1\ (j,k)] \times [F_2\ (j-m,k-n)]$ term in the equation is the cross correlation coefficient between the two images, large value of cross correlation indicates small offset values.

Interferometry is only possible when there is overlap of ground reflectivity with atleast two antennas. Orbital baseline estimation is done for the understanding of the relationship between the orbits of master and slave images. When the perpendicular component of the baseline B_{prep} increases beyond a certain limit known as critical baseline no phase information is preserved, coherence is lost and interferometry is not possible. The critical perpendicular baseline $B_{prep,cr}$ is calculated as follows (SARscape, 2010):

$$B_{prep,cr} = \frac{\lambda\, R\ \tan(\theta)}{2\ R_r} \tag{9}$$

where λ is the wavelength, R is the range distance, R_r is the pixel spacing in range and θ is the incidence angle.

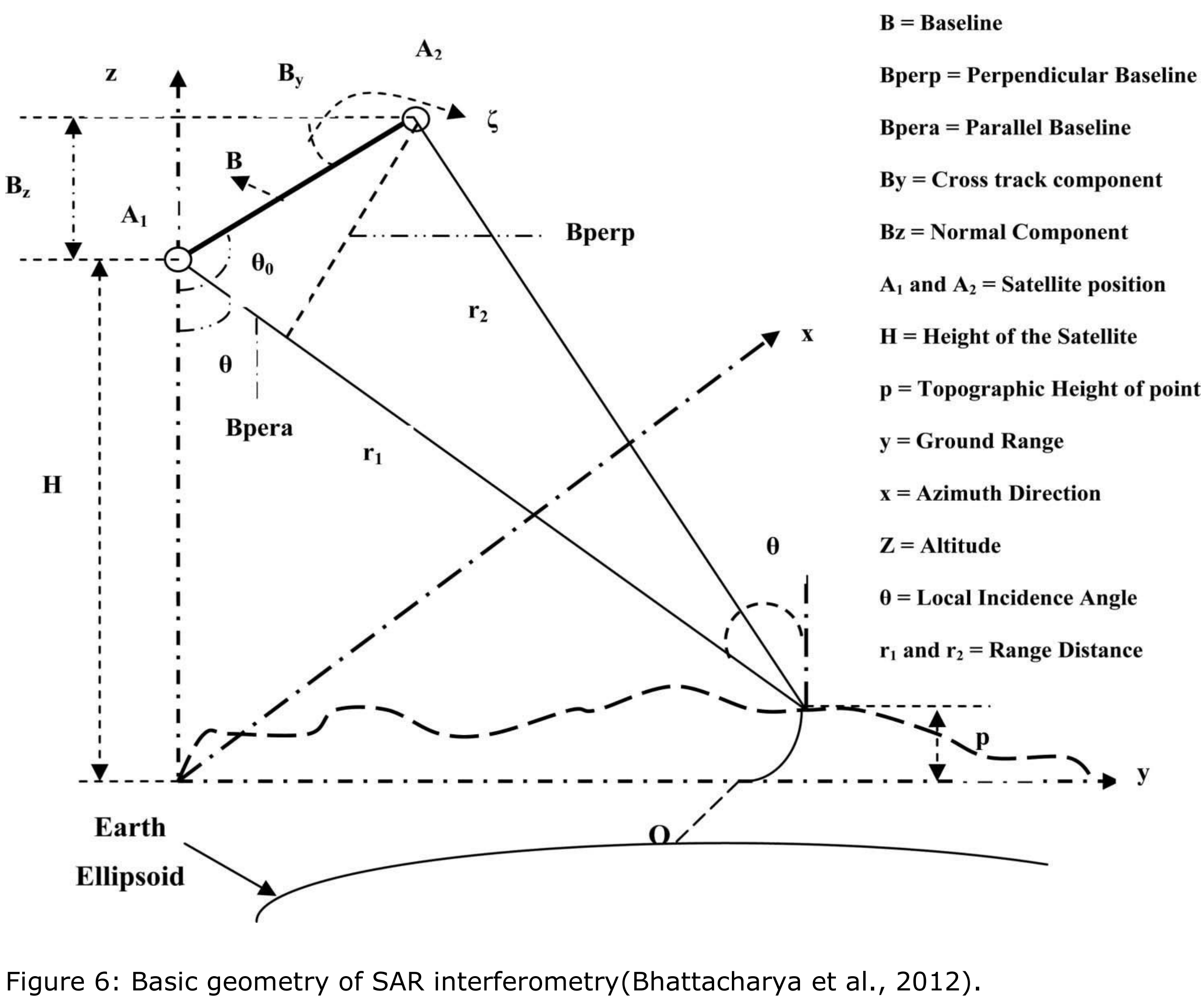

Figure 6: Basic geometry of SAR interferometry(Bhattacharya et al., 2012).

A complex interferogram is generated by the pixel by pixel multiplication of master and complex conjugate of the slave image(Bhattacharya et al., 2012).

$$F_1 \ F_2^{\ *} = |F_1| \ \exp(j\phi_1) \ |F_2| \ \exp(\mathrm{j}\,\phi_2) = |F_1| \ |F_2| \ \exp[j(\phi_1 - \phi_2)] \qquad (10)$$

where in equation (10), F_1 and F_2 are the pixel values of master and slave images and phase difference is represented as $\phi_p = \phi_{1p} - \phi_{2p}$. This phase difference is represented as fringes of a interferogram, the phase difference includes topography and horizontal or vertical displacement. Fringes are represented by rainbow colors where each cycle of color represent a phase change of 2π, also the order of the appearance of colors tell that weather the displacement is towards the line of sight or away from it.

The interferometric phase is affected by flat earth that means the objects having same height donot possess the same interferometric phase. Further due to the flat earth effect the fringe density is also high so it is necessary to flatten the interferogram before the process of phase unwrapping. The model used for interferogram flattening is given in the equation (11)(Bhattacharya et al., 2012).

$$\delta\phi^{flat} \cong -\frac{4\,\pi}{\lambda} \ B \ \sin(\theta_0 - \zeta) = -\frac{4\pi}{\lambda} \ B_{para} = -\frac{4\pi}{\lambda} \ [|(\bar{O} - \overline{A_1})| - |\bar{O} - \overline{A_2}|\,] \qquad (11)$$

Coherence is the degree of degree of the quality of interferometric phase and the measure of correlation. It is estimated using flattened interferogram and the intensity image. The coherence for a pair of images is given by(Small et al., 1993).

$$\gamma = \left[\left[\frac{1}{N} \sum_{1}^{N} F_1 \, F_2^{*}\right] / \sqrt{\frac{1}{N}\sum_{1}^{N}|F_1|^2} \ \sqrt{\frac{1}{N}\sum_{1}^{N}|F_2|^2} \right] \qquad (12)$$

where N is the number of looks. Coherence is a unitless and its value ranges between 0-1 with grey shade images. White represents high correlation value of 1, whereas black represents 0 low correlation value. The coherence value of less than 0.25 is not suitable for the process of phase unwrapping. The value of coherence can be increased by using adaptive filters(Bhattacharya et al., 2012).

The interferometric phase is measured in the interval of $(-\pi, \pi)$. The phase difference of two images lead to 2π ambiguity, for the purpose of converting the phase to height or displacement absolute value of phase at each pixel is required. The process of phase unwrapping is estimating the total phase from wrapped phase by restoring a correct multiple of 2π to each pixel depending on the number of wavelengths that have elapsed in the total path length of the SAR signal returning to the antenna(Pellika et al., 2009).Phase unwrapping is the critical factor determining the accuracy of SAR interferometry.

Several algorithms are available for the process of phase unwrapping like region growing and minimum cost flow. Minimum cost flow is better where we have large areas with low coherence but the computational time is high(Bhattacharya et al., 2012).

The process of refinement and reflattening refines the orbits by getting absolute phase value to remove the phase offsets over the nonmoving areas or surface positions that are not affected by ground displacement. A Ground Control Point (GCP) file is used to remove the inaccuracies in the orbits. After this process the unwrapped phase information can be used for transformation into height or displacement values(SARscape, 2010).

The actual height was estimated using a polynomial function to model the phase to height relation given by the equation (13)(Small et al., 1993;Bhattacharya et al., 2012)

$$h = \sum_{i=1}^{M} c_i \ \emptyset_e^{i-1} \tag{13}$$

where c_i is the polynomial coefficients $\{c_1, \dots, c_M\}$, $\emptyset_e^{i-1}$ is the reflattened phase value of the pixel and h is the actual height of the pixel.

For the estimation of the displacement values the key factor is the angle α i.e. the angle between the radar Line Of Sight (LOS) and the direction of the glacier motion. It can be calculated by the equation (14)(Li et al., 2008).

$$\cos\alpha = \cos\theta \ \sin S + \sin\theta \ \cos S \ \cos\varphi \tag{14}$$

where θ is the incidence angle, S is the surface slope, φ is the relative azimuth angle between the two directions.

The magnitude of the displacement D can be derived using the equation (15)(Li et al., 2008)

$$D = \frac{\Delta l}{\cos\alpha} = \frac{N_{fr} \times \lambda}{2 \times \cos\theta \ \sin S + \sin\theta \ \cos S \ \cos\varphi} \tag{15}$$

where Δl is the displacement along the LOS, λ is the wavelength, N_{fr} is the number of fringes along the area of interest. For the estimation of the glacier flow following assumptions are made: (a) glacier flows parallel to surface bed rock,(Kumar et al., 2011)
(b) DEM provides the terrain surface topography of the glacier, (c) surface elevation change between the two acquisitions is negligible, (d) the atmospheric effect is negligible(Li et al., 2008). All these assumptions are made to drive glacier flow pattern using InSAR technique.

3 RESEARCH METHODOLOGY

This chapter explains the research methodology for the purpose of glacier classification and estimation of the movement. Section 4.1 explains how the different zones of the glacier are identified using multitemporal SAR images and use of polarimetric decompositions for classification by Support Vector Machines. Section 4.2 give the background details of displacement map obtained by differential SAR interferometry and feature tracking techniques using SAR and optical images.

3.1 Glacier Classification

3.1.1 Discrimination of Glacier Facies using Multi-Temporal SAR Images

Different zones of glacier, described in section 2.4.3, have different scattering mechanisms which vary with season. Glacier facies can be identified by the use of multi-temporal SAR images(Patrington, 1998). As SAR backscatter values depend on the incidence angle and the wavelength of the signal therefore acquired images should be of the same sensor and with an identical geometry. The approach adopted for glacier facies identification is to combine SAR images from three different season winter, early summer and late summer i.e. end of melt season. These suitable Single Look Complex (SLC) SAR images have to be multilooked, georeferenced, filtered and terrain corrected using a Digital Elevation Model (DEM) to remove the effects of layover and shadow. Finally these images are stacked creating a single three band image in which blue channel is assigned to winter image, red channel to summer image and green channel to late summer image to display the multi-temporal signatures as distinctive colors(Patrington, 1998).

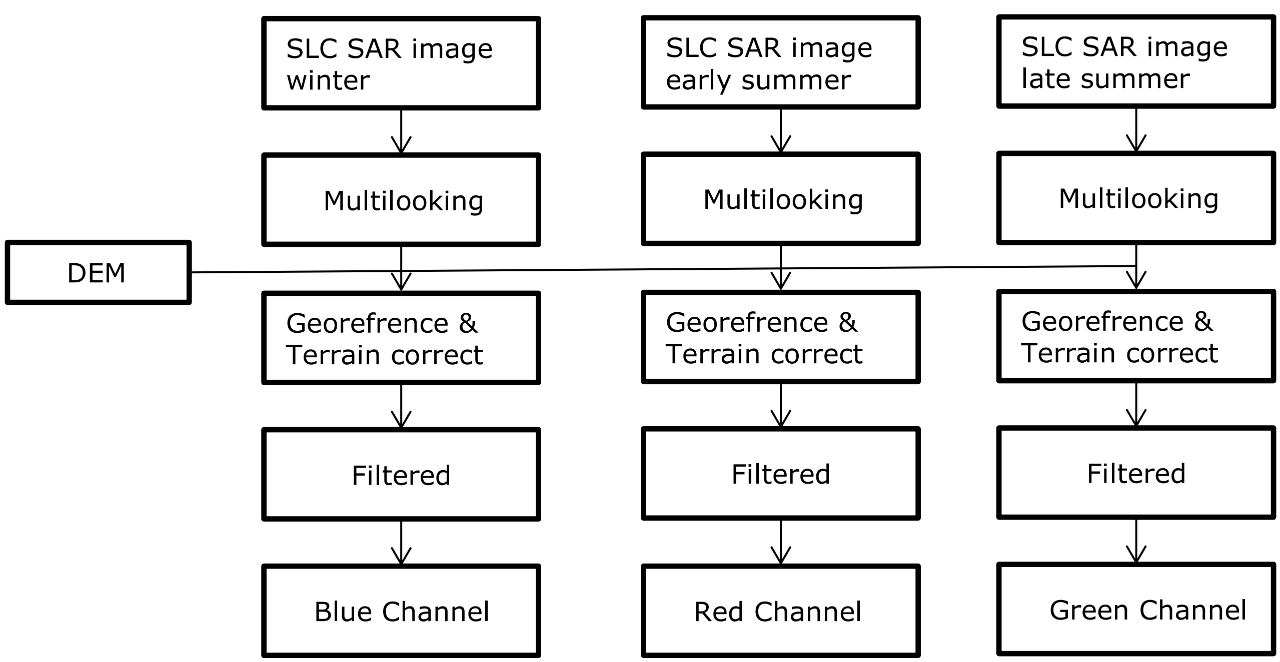

Figure 7: Diagram for glacier facies discrimination using multi-temporal SAR data

3.1.2 Polarimetric Decompositions

The electric and magnetic field vectors of an electromagnetic (EM) wave are perpendicular to each other this is known as transverse nature of EM waves. The vectorial nature these transverse waves is called polarimetry. When the EM wave hits the target it interacts with it a part of incident wave is absorbed and the rest is radiated back as a new EM wave. The properties of these radiated waves are different and can be used for identification of the scatters. The purpose of decomposition is to discriminate between volume and surface scatters. If target is pure it is considered as coherent and incoherent is case of distributed scatters. Different zones of a glacier can be identified with the help of polarimetric decompositions as the scattering mechanism varies from volume to surface scattering depending upon the type of snow pack.

3.1.2.1 Pauli Decomposition

It is a coherent decomposition that expresses the scattering matrix as a complex sum of Pauli matrices(Cloude et al., 1996).

$$S = \begin{bmatrix} S_{HH} & S_{HV} \\ S_{VH} & S_{VV} \end{bmatrix} = \frac{a}{\sqrt{2}}\begin{bmatrix} 1 & 0 \\ 0 & 1 \end{bmatrix} + \frac{b}{\sqrt{2}}\begin{bmatrix} 1 & 0 \\ 0 & -1 \end{bmatrix} + \frac{c}{\sqrt{2}}\begin{bmatrix} 0 & 1 \\ 1 & 0 \end{bmatrix} + \frac{d}{\sqrt{2}}\begin{bmatrix} 0 & -j \\ j & 0 \end{bmatrix} \qquad (16)$$

S is the scattering matrix, a, b, c and d are complex and given by:

$$a = \frac{S_{HH}+S_{VV}}{\sqrt{2}},\; b = \frac{S_{HH}-S_{VV}}{\sqrt{2}}, c = \frac{S_{HV}+S_{VH}}{\sqrt{2}}, d = j\frac{S_{HV}-S_{VH}}{\sqrt{2}} \qquad (17)$$

For monostatic radars $[S_{HV}]$=$[S_{VH}]$, that leads $d = 0$

Span value is given by:

$Span = |S_{HH}|^2 + |S_{VV}|^2 + 2|S_{HV}|^2 = |a^2| + |b^2| + |c^2|$
(18)

$|a^2|$ determines the power scattered by targets characterized by single or odd bounce, $|b^2|$ determines the power scattered by targets characterized by double or even bounce, $|c^2|$ determines the power scattered by targets that return orthogonal polarization i.e. volume scattering(Huang et al., 2011).

3.1.2.2 Eigen Vector-Eigen Value Decomposition

A non-zero vector x is eigenvector of a square matrix A if there exists a scalar λ i.e. Ax = λx where x is eigenvector and λ is the eigenvalue. Scattering matrix can only characterize coherent or pure targets, 3x3 hermition coherency matrices are used to identify impure targets.

The coherency matrix is decomposed as follows:

$$\langle[T_3]\rangle = [U_3][\Sigma_3][U_3]^{-1} \qquad (19)$$

The 3x3 diagonal matrix contains the eigenvalues of $\langle[T_3]\rangle$

$$[\Sigma_3] = \begin{bmatrix} \lambda_1 & 0 & 0 \\ 0 & \lambda_2 & 0 \\ 0 & 0 & \lambda_3 \end{bmatrix} \quad (20)$$

Where $\lambda_1 > \lambda_2 > \lambda_3 > 0$

The 3×3 unitary matrix $[U_3]$ contains eigenvectors $\underline{u}_i$ for $i = 1, 2, 3$ of $\langle [T_3] \rangle$

$$[U_3] = [\underline{u}_1 \ \underline{u}_2 \ \underline{u}_3] \quad (21)$$

The interpretation of scattering mechanisms is given by Eigen vectors of the decomposition of $\underline{u}_i$ for $i = 1, 2, 3$ id defined as follows(Cloude et al., 1997).

$$\underline{u}_0 = \sqrt{\lambda} \left[\cos \underline{\alpha} \quad \sin \alpha \cos \underline{\beta}\, e^{\underline{j\delta}} \quad \sin \alpha \cos \underline{\beta}\, e^{\underline{j\gamma}} \right] \quad (22)$$

Secondary parameters are the function of the eigenvalues and eigenvectors of $\langle [T_3] \rangle$

Entropy(H): - Its value ranges from 0 to 1, represents the randomness of the scattering mechanism. H=0 in case of isotropic scattering and $H = 1$ for totally random scattering and defined as follows(Lee et al., 1999):

$$H = -\sum_{i=1}^{3} p_i \log_3(p_i) \quad (23)$$

Alpha $(\underline{\alpha})$:- It is the main parameter for the identification of the dominant scattering mechanism. Its value ranges from 0 to 90°, $\underline{\alpha} = 0$ for surface scattering, $\underline{\alpha} = 45°$ dipole scattering, $\underline{\alpha} = 90°$ for double bounce scattering. It is defined as follows(Huang et al., 2011):

$$\underline{\alpha} = \sum_{i=1}^{3} p_i \ \alpha_i \quad (24)$$

Anisotropy(A): - It is the complementary parameter to polarimetric entropy and is the measure of the relative importance of second and third eigenvalues. This parameter is very useful in distinguishing different scattering process when entropy reaches high value. It is defined as follows(Lee et al., 2009):

$$A = \frac{\lambda_2 - \lambda_3}{\lambda_2 + \lambda_3} \quad (25)$$

3.1.3 Support Vector Machines

SVMs are statistical learning algorithms which work on the principal that better a better solution can be found by minimizing the upper bound on the generalization error(Camps-valls et al., 2004). A pixel is represented in a N dimensional vector, where N is the number of spectral bands.

Nonlinear classification is considered (refer to chapter 2.5). Gaussian Radial Basis Function (RBF) is used to map the classes in a higher dimension to find an optimal separating hyperplane. This function is widely used in remote sensing applications and is described in equation (26)(Huang et al., 2011)

$$K\left(x_i, x_j\right) = \exp\left(-\gamma\left\|x_i - x_j\right\|^2\right) \tag{26}$$

Parameter selection is an iterative process. The penalization parameter C must be tried exponentially good results are achieved with C in the range of $[1, 100]$, another parameter is standard deviation σ RBF works better with $\sigma \in [0,\ 0.4]$(Camps-valls et al., 2004).

3.2 Velocity Estimation

3.2.1 InSAR

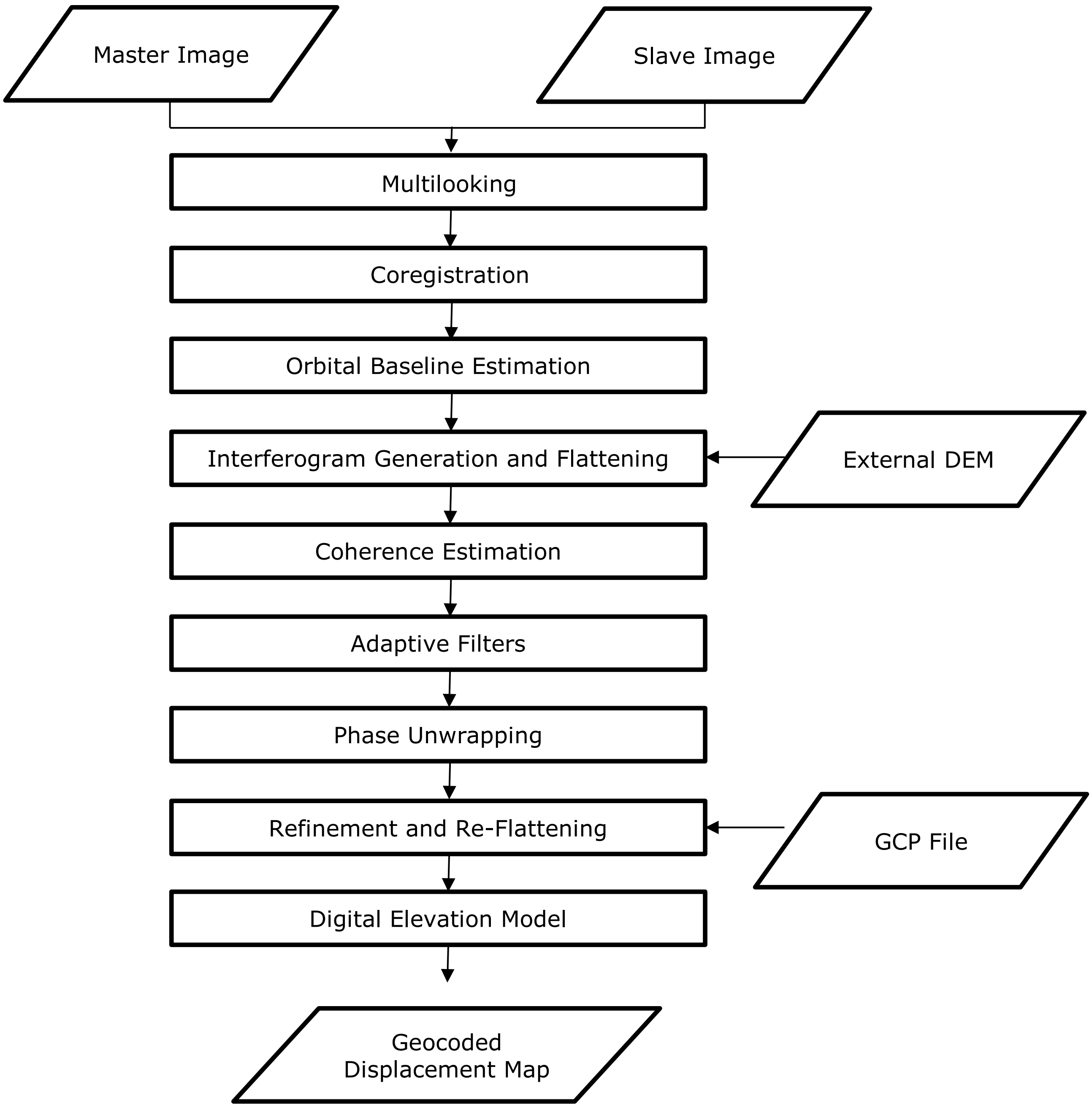

Figure 8: SAR Interferometric processing chain

The imported Single Look Complex (SLC) datasets with pre-event as master and post-event as slave are used for the process of SAR interferometry. As radar data has different resolutions in range and in azimuth direction so multilooking has to be performed to form corresponding square pixels. The multilooked images are coregistered using an accurate DEM with a subpixel level accuracy to reduce the loss of coherence due to pixel shift. Baseline is estimated after the process of coregistration. Interferogram is generated by pixel by pixel phase difference from the master and slave images. The next step is the flattening of the interferogram to remove the additional fringes due to the topographic information. Coherence is estimated and filtered using adaptive filters using similarity mean factor, identifying pixels with similar backscatter values in the master and slave images and a new pixel that falls in the range is used with a region growing approach (SARscape, 2010). A coherence threshold of 0.25 is only used for the process of phase unwrapping. In the process of phase unwrapping a modulo of 2π is added to every pixel. The orbits are refined to get the absolute value of phase using a Ground Control Point (GCP) file. The refined unwrapped phase values are converted to Geocoded displacement map using a DEM.

3.2.2 Feature Tracking

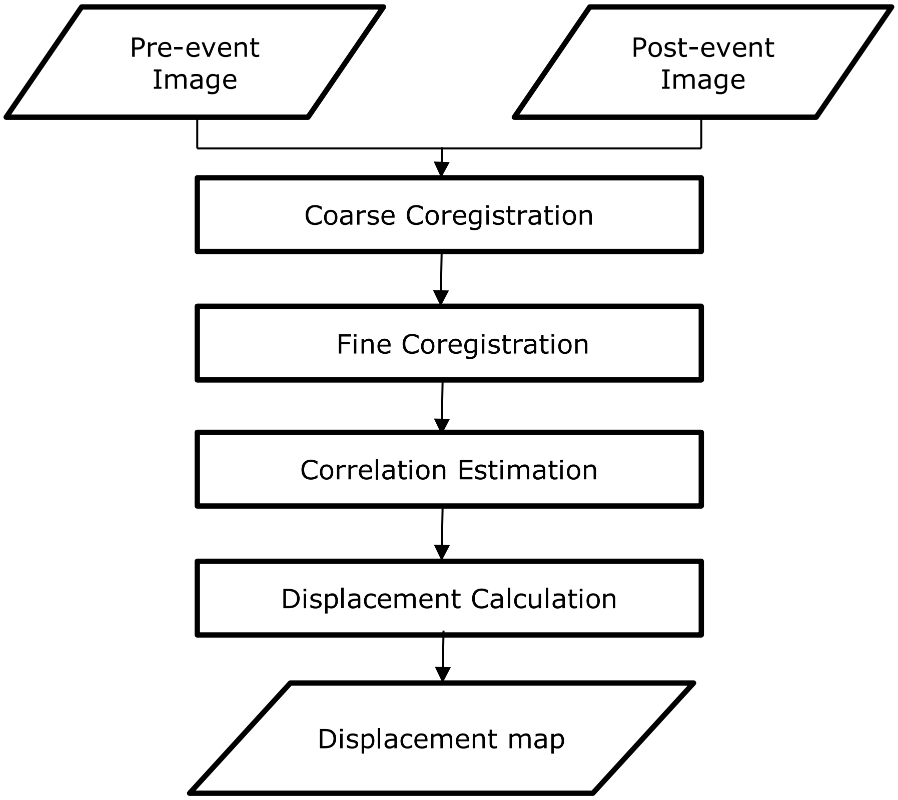

Figure 9: Methodology proposed for SAR feature tracking.

Although Differential SAR interferometry maps the displacement at a centimeter level accuracy this approach has certain limitations(Strozzi et al., 2002). SAR interferometry has constraints of having limited availability of suitable number of scenes at a certain time period(Giles et al., 2009). SAR interferometry is highly dependent on the coherence; the large temporal resolution between the two SAR acquisitions can lead to total loss of coherence. Metrological and flow conditions also affect coherence in the SAR images. Metrological sources of decorelation are snow and ice melt conditions, snowfall, wind causing the redistribution of snow and rapid motion in surge glaciers(Strozzi et al., 2002). Furthermore the interferometric velocity patterns are the representation of a certain time period only and extrapolation to retrieve annual velocities is difficult(Scherler et al., 2008).

An alternative robust approach for deriving glacier velocity feature tracking(Zongli et al., 2012). Feature tracking can use SAR and optical datasets to analyze glacier velocity over longer time periods(Scherler et al., 2008). There are some prerequisites of feature tracking (a) Surface features must be detected in both pre-event and post-event image. (b) The datasets must be accurately coregistered. (c) The spatial resolution must be less than the displacement(Huang et al., 2011).

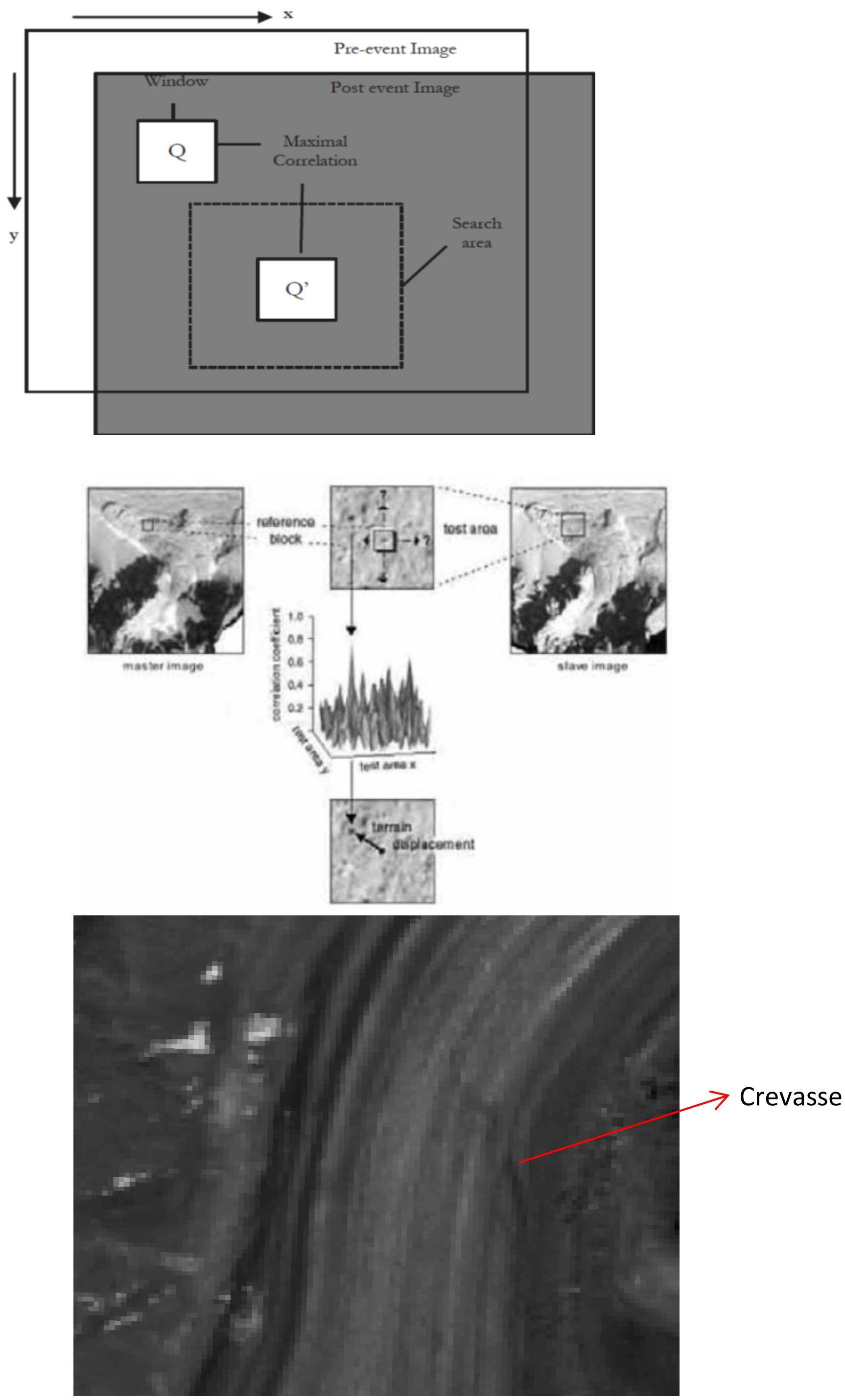

Figure 10: SAR feature tracking(Huang et al., 2011) Cross correlation for identifying identical features

SAR feature tracking is implemented by offset tracking procedures like intensity tracking and coherence tracking.

Intensity tracking: - The cross correlation of image patches are detected on SAR intensity images. The local image offsets are dependent on the presence of the identical features in the two SAR images. In areas where high value of coherence is retained speckle pattern of two images are correlated and intensity tracking is performed with high level of accuracy.
Incoherent intensity tracking is also possible but large image patches are required(Strozzi et al., 2002).

Coherence tracking: - In this method throughout the Single Look Complex (SLC) small data patches are selected and small corresponding interferogram are generated by the changing offset. Then the coherence value is estimated, the location where the degree of coherence is maximum is identified at sub pixel accuracy. Unsuitable patches are rejected by the magnitude of the relative coherence value in the offsets(Strozzi et al., 2002).

For optical images, one pre-event and other post-event coregistered images with high temporal resolution are used. The pre-event image is divided into grids and a search window is defined, which searches the similar counterpart in the post event image. The cross correlation peak finds the exact match and the displacement is determined.

Coregistration and Correlation coefficient

Coregistration is the pixel by pixel matching and correlation is the degree of matching in pre-event and post-event image. The cross correlation coefficient is given by the equation (27)(Evans, 2000).

$$CCC(u,v) = \frac{\sum_{x,y}\Big((f(x,y)-\bar{f}) \times \big((g(x+u,y+v)-\bar{g}(x+u,y+v))\big)\Big)}{\sqrt{\sum_{x,y}\Big((f(x,y)-\bar{f})\Big)^2}\sqrt{\sum_{x,y}\big((g(x+u,y+v)-\bar{g}(x+u,y+v))\big)^2}} \tag{27}$$

here $f(x,y)$ and $g(x,y)$ are the pixel values in window Q and Q' of pre-event and post-event images. u and v are the offsets between Q and Q', $\bar{f}$ and $\bar{g}(u,v)$ are the average pixel values of Q and Q'. The correlation window should be large enough to accommodate largest possible displacement.

Displacement Calculation

The center coordinate window Q and correlated window Q' is (x, y) and $(x + \Delta x, y + \Delta y)$ respectively. Then the displacement is calculated as follows:

$$D_h = \sqrt{(R_x \Delta x)^2 + \left(R_y \Delta y\right)^2} \tag{28}$$

where R_x and R_y are the pixel spacing in x and y directions. For SAR data they are represented as azimuth and slant range directions.

The high relief topography reduces the visibility of the valley glaciers for the side looking radars(Trouvé et al., 2007). Also optical images have a limitation in cloudy conditions which are persistent over a long time over glaciers(Scherler et al., 2008). The images with different incidence angle leads to distortion even for the same area. The images which are correlated the resulting offsets in the image lines and columns is also due to misregistration, topographic effects, orbits and altitude so all these factors must be removed for the accurate calculation of the glacier flow(E. Berthier et al., 2005). An accurate DEM must be used for the purpose of orthorectification(Trouvé et al., 2007). The most important step in feature tracking is to find the correlation coefficient, the search window with a high value of correlation coefficient are used to find the displacement(Anukesh, 2013). The expected accuracy of offset feature tracking is about 0.1 of the pixel size(Huang et al., 2011).

4 STUDY AREA DATASETS AND DATA DISCRIPTION

4.1 Study Area

This study concerns the Samudra Tapu glacier which is located in the Great Himalayan range of North-West Himalaya; district Lahaul Spiti in the northern state of Himachal Pradesh.
Among the 200 glaciers in the Chandra-Bhaga basin it is the second largest glacier in the upper Chandra basin. The accessibility to Samudra Tapu is through Rohtang pass at 3915 m altitude, therefore the region is region is cutoff from the rest of the world for most part of the year. The region consists of intersecting mountain ridges and is heavily glaciated. Most of the precipitation is in the form of snow and very cold alpine glacial climate(Shukla et al., 2010).

Samudra Tapu glacier forms a cirque at high elevations and flows like a valley glacier in the lower altitudes in the west- east direction. The glacier is confined between latitudes 32°24′0″N to 32°32′45″N and longitudes 77°22′30″E to 77°32′30′′E with elevation ranging from 4200 m to 6000 m above mean sea level and about 10 km south-west of famous Chandra Tal lake. The total area occupied by the glacier is estimated using the Survey of India topographic maps no. 52H/6, 52H/7, 52H/10 and 52H/11 which are of scale 1:50,000 scale made in 1962 was 94.36 km^2.This boundary was modified using the Landsat September 2013 image for the ablation season and the areal extent has reduced to 91.86 km^2. The areal extent estimated by Kulkarni et al. (2006) is 73 km^2 for the year 1962 this is due the non-inclusion of the North West region of the glacier. The total recession of the glacier is about 800 m from the year 1962 to 2013 with an average retreat of 19.5 m per year.

Table 1: Changes observed in Samudra Tapu glacier(Kulkarni et al., 2006)

Stage	Lowest elevation (m)	Glacial length (m)	Area (km^2)
1962-1993	4100	20161	77.67
1993-1998	4120	18280	77.06
1998-2000	4160	17163	76.03

At the snout of the glacier there is a moraine dammed lake whose extent is continuously changing with the further melting of the glacier. There is change in the shape and the orientation of the lake with respect to the change in the snout in the successive years. The region consists of flood plain of the deglaciated valley they are suggested to be the relic terminal moraines with fluvial overprinting caused due to subsequent flooding. The rate lake extension and the associated melt is the main cause of concern to the natural environment and human settlements in the downstream(Dhar et al., 2010).

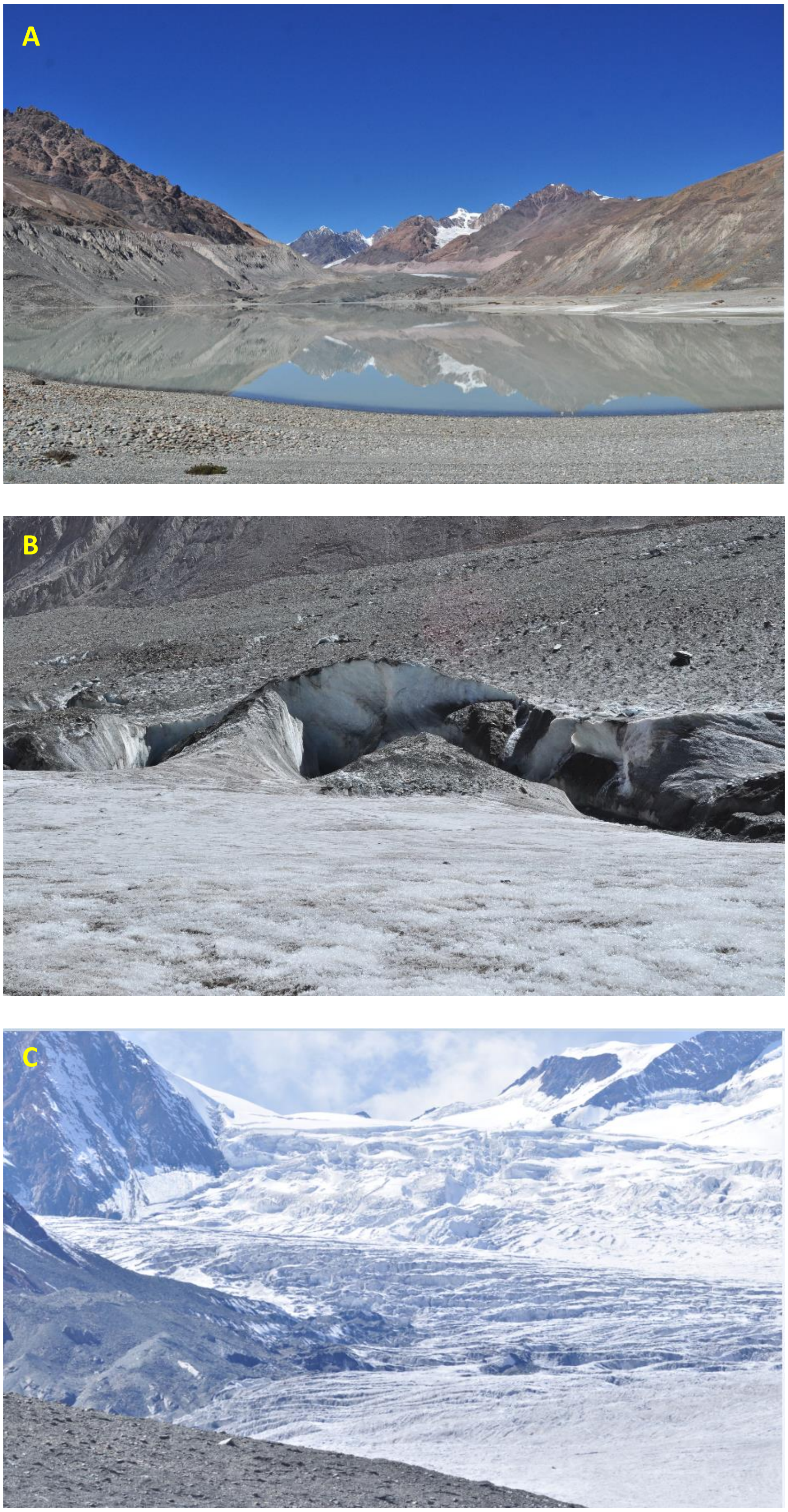

Figure 11: These photographs were taken during field visit on 3-10-2013 A) Moraine dammed lake at snout B) Supraglacial channel C) Firn.

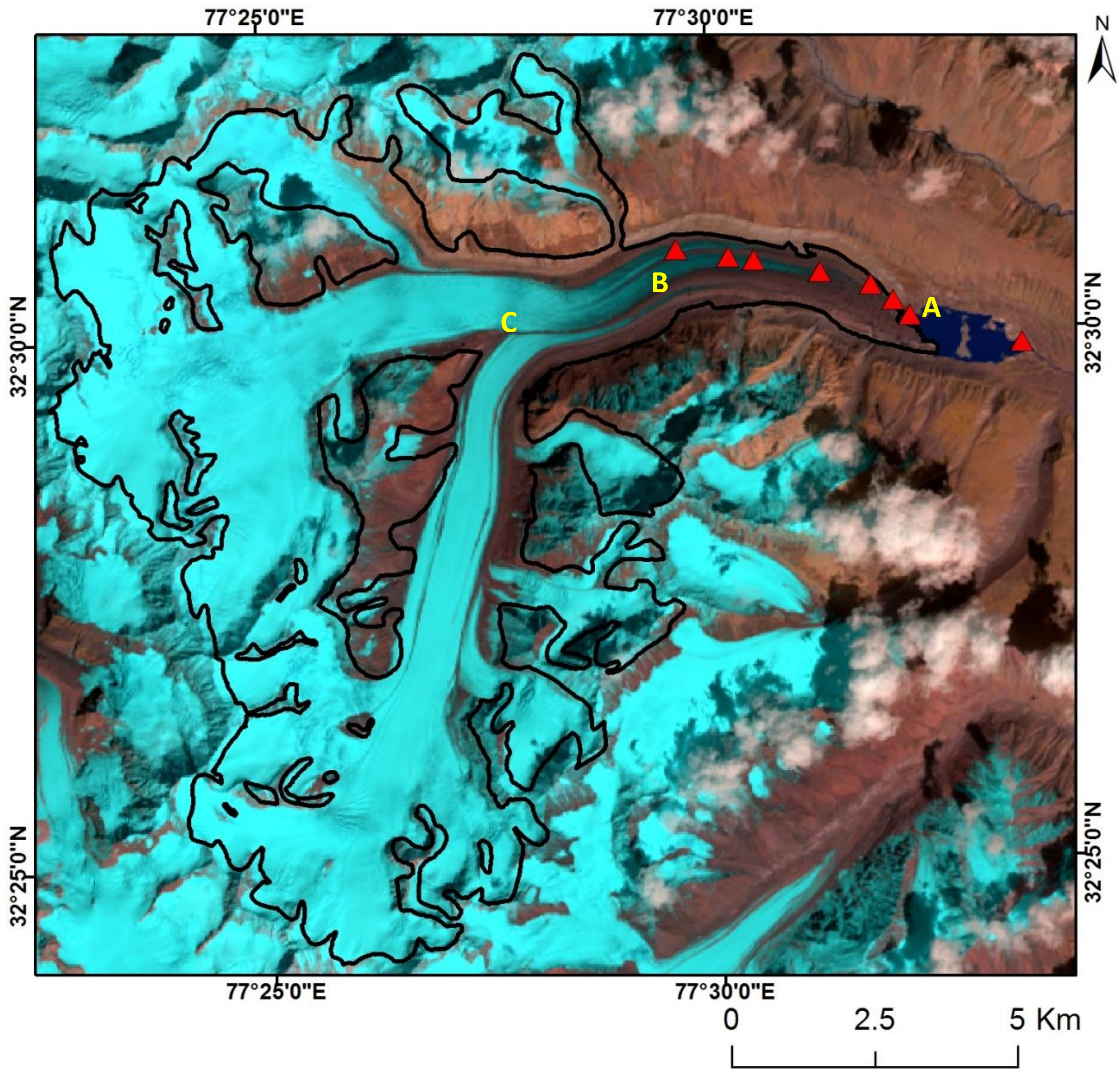

Figure 12: Samudra Tapu Glacier FCC Landsat image 25-09-2013, GPS point taken during field visit. A, B, C indicating the location of the photographs taken during field visit.

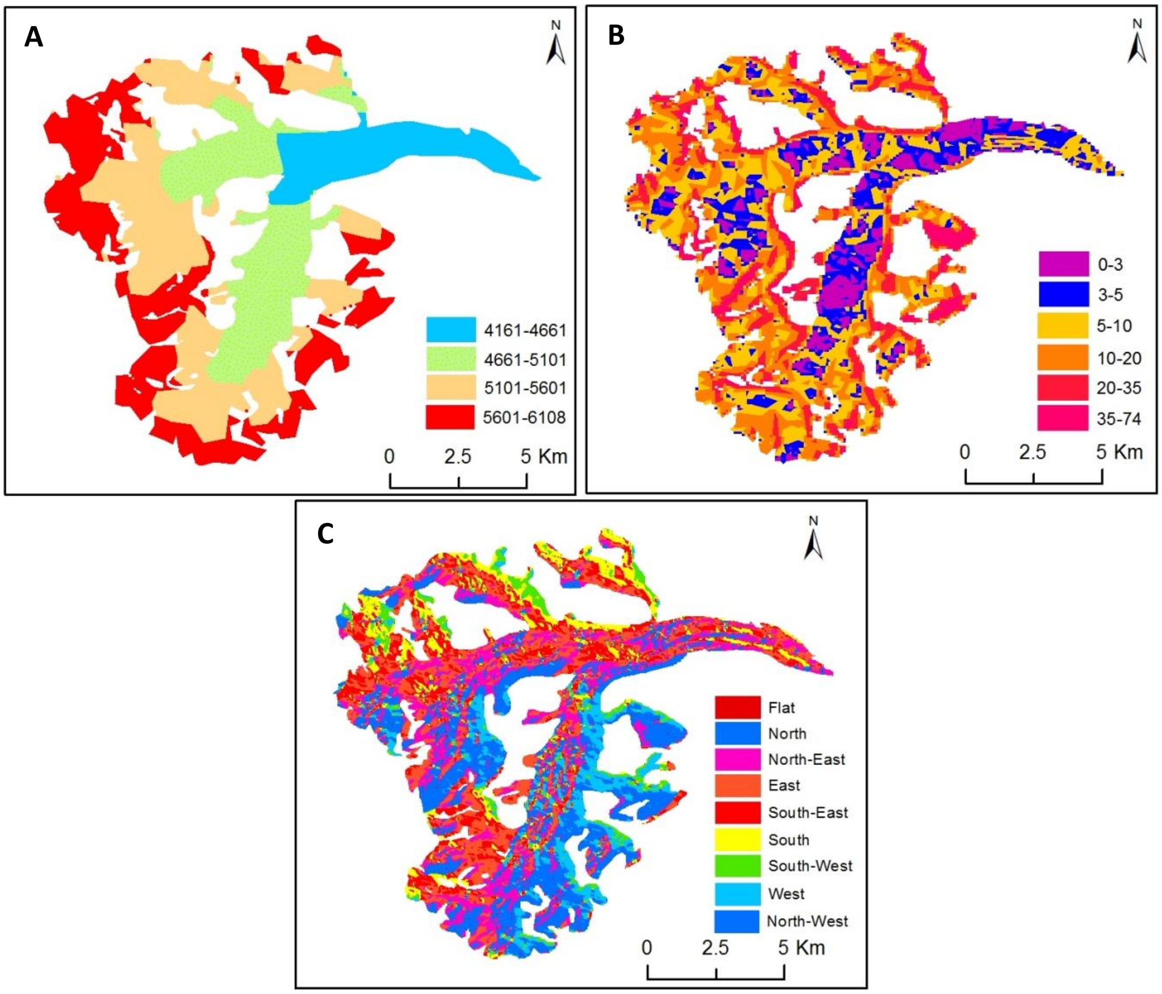

Figure 13: A) Classified elevation zones using SRTM DEM B) Aspect map using ASTER DEM C) Slope map generated using SRTM DEM

Table 2: GPS points collected during the field visit

Location	Altitude (m) MSL ht.	Latitude (North)	Longitude (East)
Lake	4174	32°29′51.1″	77°33′27.3″
Snout	4199	32°30′07.1″	77°32′12.8″
Snout 1	4215	32°30′16.0″	77°32′02.7″
Snout 2	4245	32°30′25.1″	77°31′47.2″
Damp Snow	4330	32°30′32.6″	77°31′13.2″
Crevasses	4402	32°30′40.1″	77°31′29.5″
Supra Glacial Channel	4425	32°30′42.4″	77°30′12.1″
Middle Ablation Area	4477	32°30′41.2″	77°29′37.6″

4.2 Data Description

1. RISAT-1 MRS datasets were used for the identification of glacier facies by temporal data.
2. Fully polarimetric ALOS/PALSAR and RADARSAT-2 datasets were used for the purpose of polarimetric decompositions
3. ERS 1/2 images with one day temporal resolution were used for obtaining horizontal displacement using SAR interferometric techniques.
4. TanDEM-X, RISAT-1 MRS and ALOS/PALSAR dual-polarimetric datasets were used for SAR feature tracking.
5. Landsat and Aster images were used for feature tracking of optical images.

4.3 Software

1. ENVI 5.0 and SARscape 4.4.003 for importing datasets and polarimetric decompositions, SAR interferometry and feature tracking.
2. COSSI-Corr for estimate displacement form optical images.
3. ERDAS imagine 2013 for geocoding and mosaicking of toposheets
4. ArcGIS 10.0 for the digitisation of vector boundary and zonal statistics using DEM.
5. MATLAB R2012a and Ri386 3.1.2 for SVM code and statistical modelling.

5. RESULTS

This chapter explains the various results obtained from the proposed methods for this research work. It starts with glacier classification using multi-temporal data and polarimetric decompositions; SVM is used as a classifying method for both these approaches. Estimation of glacier flow is carried out using interferometric technique and offset feature tracking procedures. Finally the rate of flow of various classified zones is evaluated.

5.1 Glacier Classification

5.1.1 Distribution of Zones

Glaciers can be classified on thermal basis as a) Polar or cold glaciers b) Temperate glaciers (GSI). Dry snow zones are only found in cold polar glaciers therefore we can say that these regions donot exists in most of the temperate glaciers found in Himalayas. For a temperate glacier the glacial ice is at melting point for the most part of year except the winters. Superimposed ice is formed when firn is below 0˚C this condition doesnot exist on temperate glaciers thus equilibrium and snow line coincide as there is no superimposed ice zone(Paterson 2000). Furthermore wet snow line is coincident with the 0˚ isotherm subsurface position of the previous year's accumulation and has no effect on sensing properties of SAR thus cannot be detected(Paterson 2000). Percolation zone and ablation zone collectively form the accumulation region of the glacier and only surface melting in these zones. The necessary condition for a region to be classified as wet snow zone is that all the deposited snow of the winter accumulation should have melted away by the end of summer(Patrington, 1998). In the end of summer both percolation and wet snow areas are melting thus we get similar backscatter characteristics so in this research percolation and wet snow facies are treated together as percolation zone as water percolates in both zones.

5.1.2 Glacier Facies Determination using Multitemporal SAR Datasets

RISAT-1 Medium Resolution ScanSAR (MRS) datasets are used in this approach. The method uses datasets from different seasons; winter, late summer and early summer for discrimination of different glacier facies or zones. The datasets are separated by multiple repeat cycle period of a satellite so that the geometry is almost identical. The imported Single Look Complex (SLC) datasets were multilooked with an azimuth looks 1 and range looks 1. For the purpose of georefrencing and terrain correction an accurate Digital Elevation Model (DEM) is required; accuracy of various DEMs was analyzed using spot height points from the toposheets and hand held GPS points collected during the field visit. ASTER DEM with a spatial resolution of 30 m had minimum error in the terms of vertical accuracy so this DEM is used throughout this research. The multilooked images were georeferenced with ASTER DEM and resampled at 18 m grid spacing. The area having the layover and shadow errors was removed from the images as it can lead to classification errors. SAR images have to be filtered to remove the speckle noise, for speckle filtering

Equivalent Number of Looks (ENL) has to be estimated from the smooth part of the image where variance of signal is low thus the main contribution is from speckle, so the moraine dammed lake at the snout of the glacier was used to calculated the ENL number and was calculated as(Torres et al., 2012)

$$ENL = \frac{1}{Coff.\ of\ variation^{\,2}} \tag{29}$$

The georeferenced images were filtered using Lee filter and ENL number was specified.
The filtered images are converted to backscatter file in decibel (db.) units by using formula $10 * alog\ (float\ (b))$; where b is the georeferenced filtered image. The images were merged by creating a single three band image in which blue channel to winter image, red channel to early summer image and green channel to late summer image was assigned.

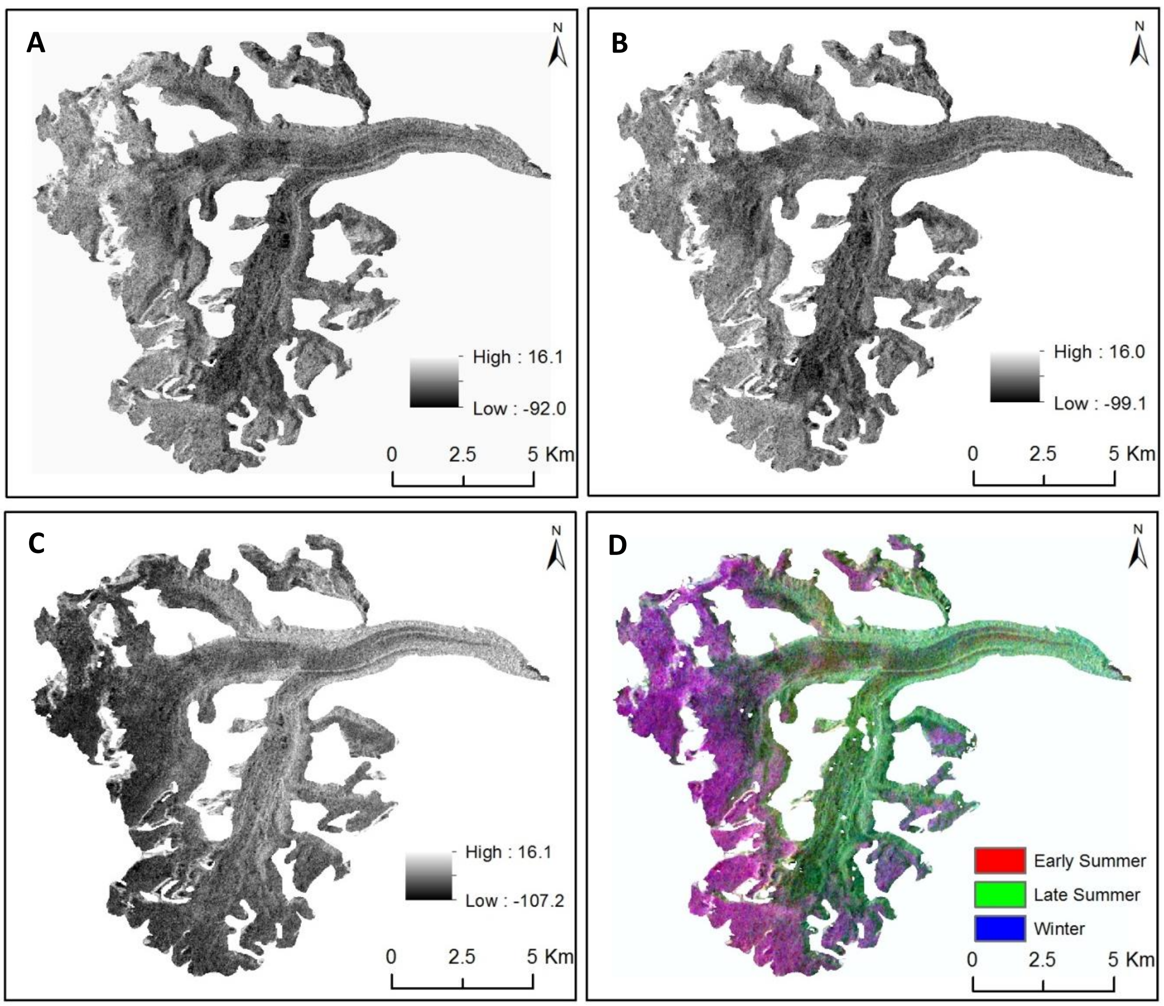

Figure 14: A), B), C) Backscatter images with HH polarization for the date 5-January-2013, 15-April-2013 and 18-August-2013 D) Single channel RGB color composite image using multitemporal RISAT-1 MRS data with HH polarization.

Percolation zone exists at high elevations where no melting in winters and late summer, so high backscatter values are observed. But in late summer the region appears dark in color due to the melting of snow leading to low backscatter values this zone appears purple in color in the figure 14D. Also appearance of green color at higher altitude as seen in the figure 14D is quite anomalous and unusual. Partington (1998) suggests that this can be due to summer depth hoar development, rime-frost development and high winter accumulation over percolation facies. From the figure 14D we can see appearance of purple color at some lower altitudes which was unusual; these regions were identified as ice walls using the Survey of India (SOI) toposheets, ice walls give higher returns being a corner reflector. Ice Facies are just found below the percolation zone where there is melt observed in late summer and early summer but no melt is observed in the winters; low backscatter values were observed in all the seasons but due to different reasons. In winters the whole glacier is covered by dry snow, the microwave radiations are transparent to dry snow and the backscatter comes from the glacial ice a smooth surface; acts as a specular reflector causing low returns back to the radar antenna. In early summer there is little melting occurs in the winter snow, so due to the presence of moisture low backscatter values are observed. Almost all of the seasonal snow has melted away in late summer almost and the backscatter is coming from the wet firn which melts in the day time and refreezes in the night and compacts into a rough solid leading to a little higher returns in this season and also the RISAT-1 images were acquired early morning so the backscatter comes from this refreeze firn. Figure 14D shows glacial ice with a tint of green color. The regions of debris can be clearly seen further down the glacier near the snout and also as moraines which are moving along the glacial ice. In the late summer image figure 14 C all the seasonal snow has melted away and the scattering contribution is from the rocks that form the debris these appear as bright areas with green color. Using multi-temporal SAR image generalized results were obtained with only two distinctive colors i.e. green and purple but using this approach we were able to evaluate the extent of percolation zone, glacial ice and debris so we have to use polarimetric decompositions for a detailed discrimination of glacier facies.

5.1.3 Polarimetric Decompositions for identifying different type of Scatters

Fully polarimetric L-band ALOS/PALSAR and fine resolution quad-pol C-band RADARSAT-2 SAR datasets are used for decompositions.

5.1.3.1 Pauli Decompositions

The SLC images were imported; a cartographic grid size of 25 m for coarse resolution L-band data and a grid size of 10 m for the high resolution C-band data were set for further processing. Multilooking was done with a factor of 7 azimuths looks and 1 range looks for L-band datasets and an azimuth looks 1 and range looks 1 for C-band data. Georefrencing and terrain correction was done using ASTER DEM; pixels with layover and shadow were masked out. The georeferenced images were then filtered using lee filter; ENL was calculated from the coefficient of variation using similar approach as done for RISAT-1 images. The filtered images are converted to backscatter file in decibel (db.) units by using formula 10*alog (float (b)); where b is the georeferenced filtered image.

A scattering matrix $[S]$ is represented as the complex sum of the Pauli matrices which were calculated from the backscatter images of various polarizations refer to chapter 3.1.2.1 using the band math tool in ENVI. Finally Span was calculated by layer stacking the Pauli matrices to display the image in a single RGB format; where red color represents single or odd bounce scatters, blue color determines the targets characterized by double or even bounce and green color represents volume scattering.

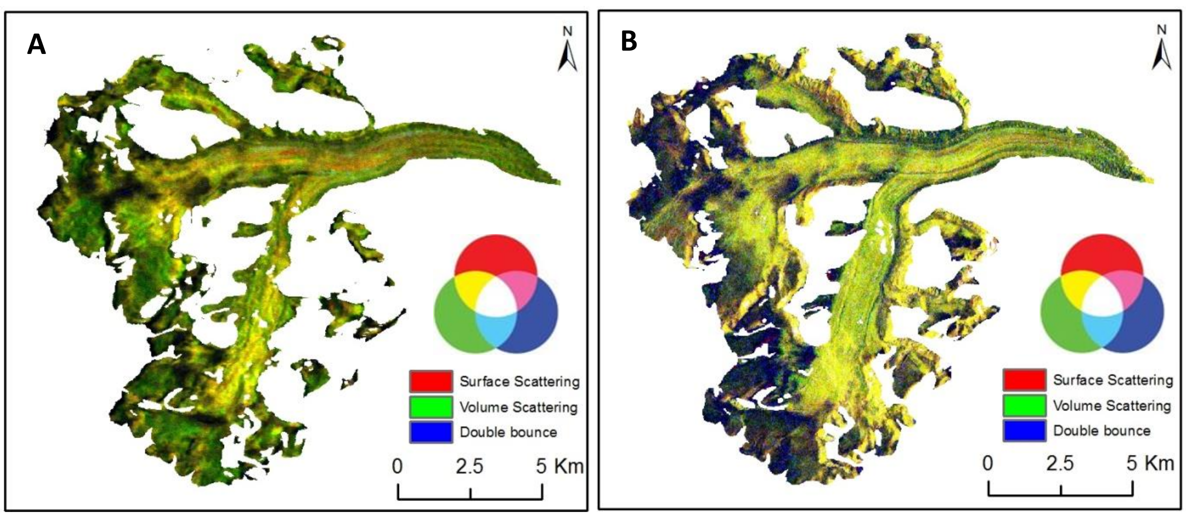

Figure 15: A) Pauli decomposition of ALOS/PALSAR B) Pauli decomposition of RADARSAT-2

ALOS/PALSAR L-band images are acquired at night time so there is much more penetration as the snow surface is dry, L-band having high wavelength are able to penetrate the dry snow and underlying features can be detected. Figure 15A shows the result of Pauli decomposition of ALOS/PALSAR data; different shades of RGB can be seen in the image. From figure 15A dark green color indicates that volume scattering is dominant at high altitudes. The microwave radiations are able to penetrate the dry snow upto a certain depth and scattering is due to the presence of volume inhomogeneities. Figure 15A shows some areas with bluish black color which indicates double bounce or even bounce scattering and the areas can be identified as ice walls. Large patches of yellow color are also seen in the figure 15A, as yellow color is the mixture of two primary colors red and green so we can say that these areas represent both scattering mechanisms i.e. surface and volume. Glacial ice is covered by a thick layer of seasonal dry snow L-band SAR signals penetrate this dry snow and ice at high ablation areas being a smooth surface reflects the radiations in a specular manner so both scattering mechanism are observed in this region. As we move down the glacier some areas are seen with red color in the figure 15A this is damp snow, the snow which melts and then refreezes in the previous year's ablation season. As the snow at lower altitudes is rough referring to chapter 2.4.2, this has more component of surface scattering thus appear red in color. Also in the figure 15A we can see bright patches of purple color these are the areas were identified as debris, they also have component of double bounce scattering mechanism but less in comparison to ice walls.

The results of Pauli decomposition of RADARSAT-2 is shown in the figure 15B, this image is of winter period. Glacier studies using SAR gives best results using winter images as no surface melting is there, the dry snow is invisible to SAR and end of ablation situation is virtually preserved(Konig et al., 2001). The Pauli decomposition of C-band RADARSAT-2 images less number of colors as compared to L-band ALOS/PALSAR data. The reason behind this is that the wavelength of C-band is less than the L-band so less penetration is observed, also the image is acquired at winter time so seasonal snow deposits are in its peak and C-band SAR signal are not able to penetrate fully the dry snow and retrieve sub surface information. At high altitudes, blue color is mostly seen in the decomposed image which shows double bounce as the dominant scattering mechanism. This is because the low wavelengths of C-band are more affected by the surface undulations and corner scattering mechanism is observed because of the undulating surfaces. Glacial ice in the figure 15B is shown with green color as C-band SAR signals are not able to fully penetrate the dry snow thus volume scattering is dominant. Red patches can also be seen in the figure 15B at similar places to L-band data these are damp snow areas buried under the dry snow, but only can be seen at low altitudes as at higher altitude the microwave penetration is less than the deposited dry snow. Areas with debris show similar reflectance to ice walls and can be seen in the figure 15B near the snout of the glacier.

5.1.3.2 Eigen Vector-Eigen Value Decomposition

Imported SLC images were used for this incoherent decomposition. SARscape tool was used for the polarimetric decompositions. A total of six images were generated as output from the decompositions, three images of RGB i.e. one for each color also entropy, α and anisotropy images were also generated. The output images were then geocoded using DEM and then color composite tool was used to enhance the colors in the image.

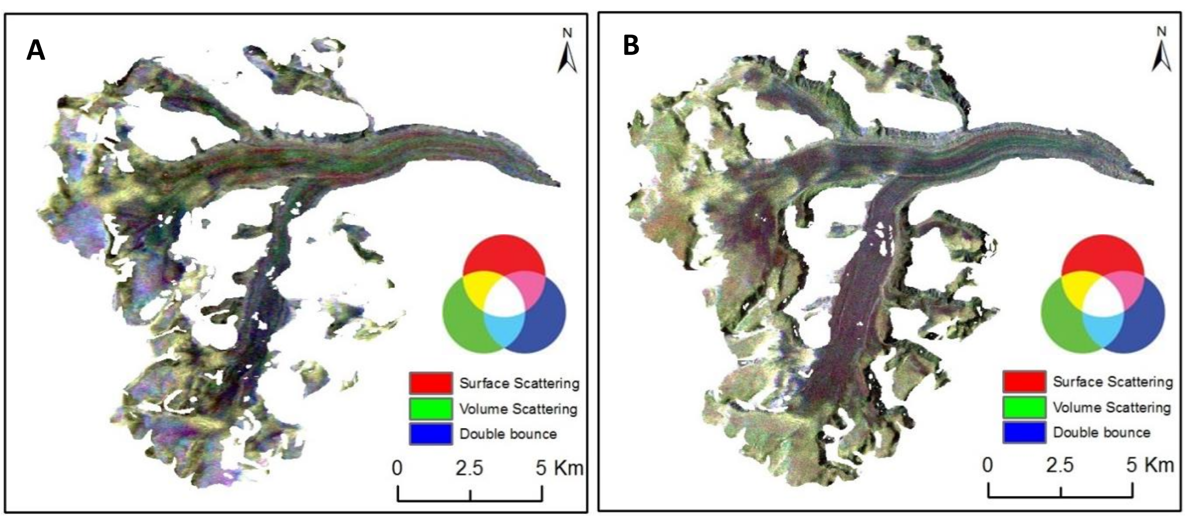

Figure 16: Eigen vector-Eigen value decomposition A) ALOS/PALSAR B) RADARSAT-2

The red, blue and green images were used to formulate a single RGB image shown in figure

15 A. The images appears different than Pauli decomposition as Eigen vector- Eigen value decompositions assume targets to be distributed scatters whereas targets are assumed to be pure in case of Pauli decomposition. The average values for angle α was found out least in percolation zone about 26.67°, but the average value rise upto be 52° in the regions with ice walls corresponding to double bounce scattering for ALOS/PALSAR datasets. Also entropy values were highest in ice walls reaching to a maximum value of 0.88 depicting a totally random scattering.

Figure 15 B shows the result of Eigen vector-Eigen Value decomposition of RADARSAT-2 datasets the difference in colors is due to the difference in penetration of SAR signals in different times of year. The average value of angle α was similar in all the different zones of the glacier and close to 45° as dominant scattering mechanism is volume scattering because of the seasonal dry snow cover. There was a slight variation in the entropy values in the range of 0.55 to 0.70, higher values are found in the regions having ice walls.

After closely examining the results of Pauli and Eigen vector-Eigen Value decomposition we can see that even though the color are different in both the images but the patterns of the appearance of the color is quite similar so we can say that a x color in Pauli decomposition and a y color in Eigen vector-Eigen Value decomposition belong to the similar zone in the glacier.

5.1.4 Classification using SVMs

Support Vector Machines algorithms are used for the purpose of glacier classification. RISAT-1 multi-temporal image and eight layers; three from Pauli decomposition, three RGB layers of Eigen vector-Eigen Value decomposition, and α, entropy images were stacked for ALOS/PALSAR and RADARSAT-2 datasets were used as input for SVM classification. SVMs are supervised learning algorithms so they require training datasets. The training samples were collected using the ROI tool in ENVI. Then the training samples were extracted from the original images and imported into Comma Separated Values (CSV) format using MATLAB. From the training sample 20% of the samples for all the classes were used to test the accuracy of the classified results. Finally R statistical software was used to implement the code for SVM; functions are already defined in R for the implementation of various kernels used in SVM's. Gaussian Radial Basis Function was used for the purpose of classification; different parameters were used in a iterative way to achieve the best classification results(Dixit et al., 2013). The classification results were having certain anomalies; a DEM was used to filter results in the following ways:

1. RISAT-1 datasets; the single band multi-temporal image shows percolation zone and ice walls with similar color so DEM was used to classify these regions as ice walls. Also the unusual appearance of green color at high altitude as referred earlier; was filtered with the help of DEM. An elevation of 5200 m was used to filter these zones.

2. Classification results of L-band ALOS/PALSAR datasets, some patches of percolation zone were appearing in the debris covered areas these were filtered using DEM. Patches of Also ice walls are fond both in percolation zone and glacial ice zone and are classified as a single class because of similar appearance but for mapping the exact extent of these zones they have to be separated into different classes by using DEM by using an elevation of 5200 m.

3. The decomposition results of RADARSAT-2 images depict debris and percolation zone with a similar tone. To prevent classification errors debris was not classified using SVM; finally of percolation DEM was used to classify the areas zone as debris; below an altitude of 5200 m. In this process the SOI toposheets were also used as an additional reference.

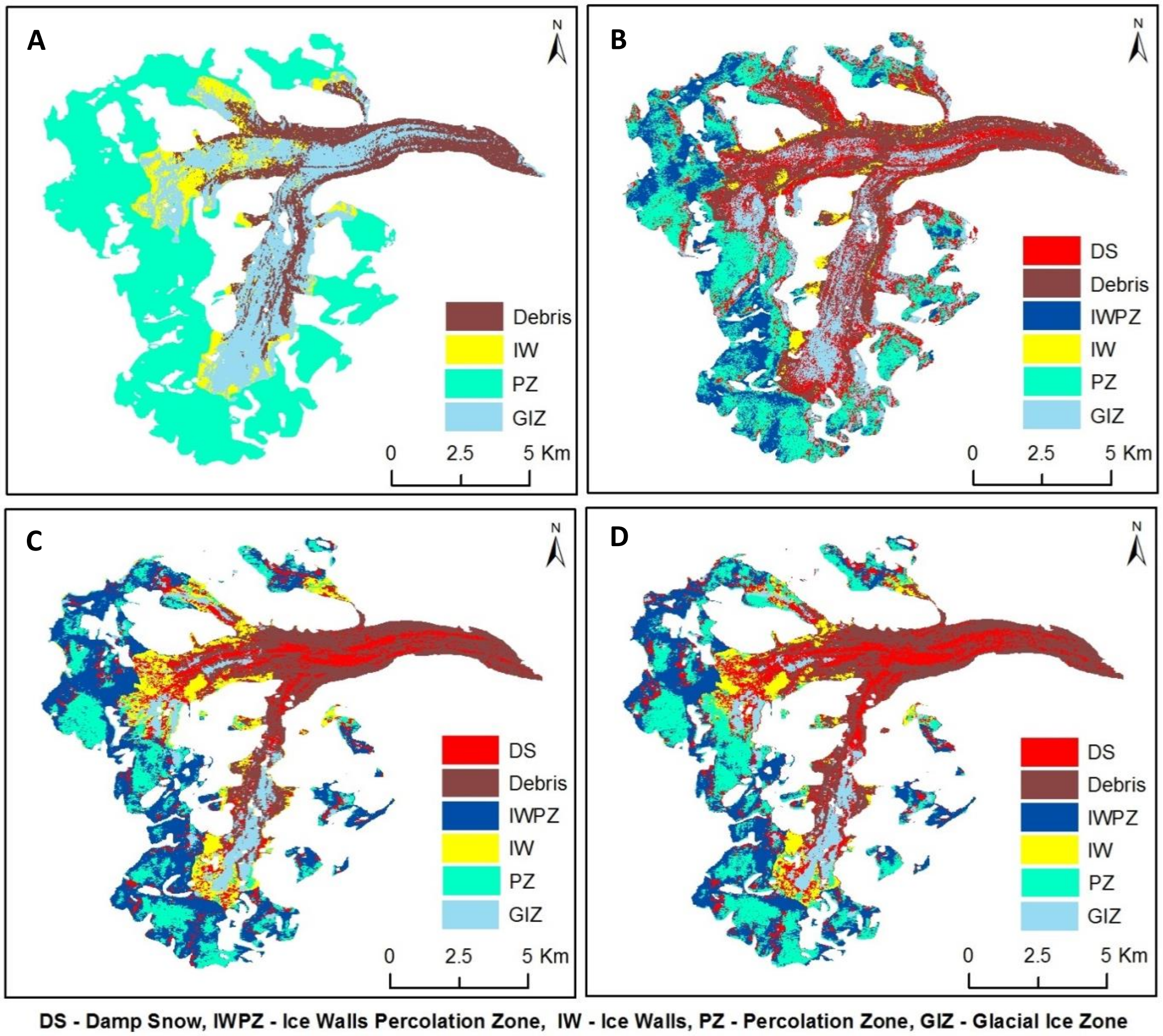

Figure 17: SVM Classification Results A) Multi-Temporal RISAT-1 dataset B) 27-January-2014 RADARSAT-2 dataset C) 06-April-2009 ALOS/PALSAR dataset D) 12-April-2011 ALOS/PALSAR dataset

Table 3: Accuracy and Kappa coefficient for different images using SVM classification

	RISAT-1 (Multi-Temporal)	ALOS/PALSAR (06-04-2009)	ALOS/PALSAR (12-04-2011)	RADARSAT-2 (27-01-2014)
Overall Accuracy	95.25%	92.70%	94.64%	93.55%
Kappa Coefficient	0.92	0.90	0.93	0.91

From the table 3 we can say that high level of classification accuracy is achieved for all the datasets, with multi-temporal RISAT-1 data having the highest value. The values of kappa coefficient are well and good for all images with 12-April-2011 ALOS/PALSAR datasets having the highest value.

Table 4: Areal extent of the classified zones in km^2 using different SAR datasets

Datasets	L/S	PZ	IWPZ	IW	GIZ	DS	Debris
RISAT-1 (Multi-Temporal)	2.90	48.06	NA	5.68	19.65	NA	13.5
RADARSAT-2 (27-01-2014)	2.20	21.72	13.50	1.73	15.14	17.20	19.97
ALOS/PALSAR (06-04-2009)	19.20	11.62	21.50	6.40	5.63	10.7	15.4
ALOS/PALSAR (12-04-2011)	19.20	15.60	17.56	4.38	4.84	14.50	14.31

ASTER Global DEM has estimated accuracy of 30 m in horizontal data so this error is inherent in the classification results as all the datasets were geocoded using Aster DEM(Japan Space Syatems, 2012).

The results from table 4 clearly suggest that the areal extent of percolation zone is highest of all the zones. In RADARSAT-2 classified image a large amount of area is classified as damp snow compared to other classified datasets. This is because of the inclusion of northern area in RADARSAT-2 images which is partially missing in ALOS/ PALSAR datasets due to the effect of layover and shadow distortions.

The all classified results are not comparable due to the difference in the amount of layover and shadow effect, different acquisition dates and dissimilar microwave frequencies used. The two ALOS/PALSAR datasets are of the same sensor and same season and thus can be compared. The RISAT-1 and RADARSAT-2 datasets are acquired using C-band radar also there is similar extent of layover/shadow in these images therefore can be used for comparison although these images are processed using different techniques.

From table 4 we can see that the two ALOS/PALSAR images of different date show a striking difference in the areal extent of classes PZ and IWPZ this may be due to variation in snow deposition patterns in both the images. Wind may change the arrangement of snow, making it more rugged therefore more pixels are classified as ice walls. There is difference in the extent of DS areas in both the images; as damp snow is formed by melting of the deposited snow from the end of ablation season of previous year. Thus varies from season to season therefore changing its overall extent in these two results.

Comparing the classification results of RISAT-1 and RADARSAT-2 images from table 4 we find that there is difference in the spatial distribution as well as total area covered by debris. As mentioned earlier in the text that DEM was used to assign the regions of percolation zone below a certain altitude as debris; due to this approach some parts of the IW are also classified as debris. Therefore debris is over estimated and IW has very less area in RADARSAT-2 image in comparison with other classification results.

Glacier is a totally dynamic system so there is difference in the areal extent of the derived classes. As discussed earlier the roughness of snow depends on its deposition and the climatic factors so there is change in the number of pixels classified as ice walls this in turn changes the spatial extent of other classes also different wavelengths are used which are affected by surface roughness. The RADARSAT-2 and ALOS/PALSAR images are acquired in time when whole glacier is covered by seasonal snow as there is difference in the penetration capabilities of different SAR systems thus difference arise in the identification of subsurface features.

The type of snow pack of a glacier varies with elevation and sun illumination so there is need to study the change in spatial extent of different classified zones with varying altitude and aspect. For this purpose the classified elevation and aspect maps were generated.

Table 5: Percentage area of classified zones in various aspects for RADARSAT-2 datasets

Aspect	Area(km^2)	PZ	IWPZ	IW	GIZ	DS	Debris
Flat	0.46	0.49	0.39	0.37	0.42	0.49	0.63
North	12.51	20.38	11.93	5.28	9.91	13.68	12.22
North-East	15.34	17.09	18.25	18.17	13.47	13.99	21.53
East	18.61	16.35	31.52	45.72	13.82	14.43	23.44
South-East	12.23	10.78	21.72	17.00	9.00	10.77	15.61
South	7.94	8.52	8.37	8.20	7.33	9.23	9.52
South-West	4.74	4.53	2.45	0.56	8.03	8.24	3.02
West	8.40	7.34	1.74	1.17	18.49	12.69	6.51
North-West	11.25	14.52	3.63	3.52	19.54	16.47	7.51

From table 5 we can see about 52% area of the PZ class lies in the northern aspects; as these areas are not much exposed to sun light thus little surface melting is observed. Half of debris covered areas are found in northern aspects this suggests that these areas receive less amount solar radiations and also due to the debris cover these vet less melting is seen in these areas. The areas of damp snow and glacial ice zone are evenly distributed among all the aspects. It’s interesting to note that about 32 % of ice walls of percolation zone and 46% of ice walls in lower regions are also found in East aspect.

Table 6: Percentage area of classified zones in various aspects for 06-April-2009 ALOS/PALSAR datasets

Aspect	Area(km^2)	PZ	IWPZ	IW	GIZ	DS	Debris
Flat	0.46	0.64	0.39	0.51	0.75	0.49	0.77
North	12.51	22.81	14.67	11.86	13.77	13.36	13.13
North-East	15.34	18.21	17.54	21.19	20.19	21.61	25.07
East	18.61	16.37	27.48	30.34	21.89	25.44	27.09
South-East	12.23	9.66	17.59	16.61	8.87	18.47	15.08
South	7.94	7.17	7.75	6.10	4.90	8.74	8.17
South-West	4.74	3.04	2.53	1.86	2.45	1.38	1.54
West	8.40	5.88	3.17	3.73	9.43	3.54	3.70
North-West	11.25	16.19	8.87	7.80	17.74	6.97	5.45

Table 7: Percentage area of classified zones in various aspects for 12-April-2011 ALOS/PALSAR datasets

Aspect	Area(km^2)	PZ	IWPZ	IW	GIZ	DS	Debris
Flat	0.46	0.68	0.36	0.50	0.90	0.36	0.82
North	12.51	21.86	13.82	13.10	13.90	12.0	13.79
North-East	15.34	19.69	16.13	22.16	18.61	21.76	25.11
East	18.61	19.42	27.11	30.73	21.30	26.78	26.76
South-East	12.23	10.32	18.86	16.88	8.52	18.78	13.79
South	7.94	6.45	8.48	6.30	4.71	8.01	8.32
South-West	4.74	2.58	2.55	1.51	2.47	1.97	1.42
West	8.40	5.10	3.14	2.01	10.76	3.86	3.97
North-West	11.25	13.92	9.55	6.80	18.83	6.48	5.99

After comparing table 5 against table 6 and 7 we can find dissimilarity in the distribution of percentage area of classes glacial ice and DS in various aspects. Difference in microwave penetration, layover and shadow distortions may be the cause of this variation. The distribution of debris in various aspects differs in RADARSAT-2 and ALOS/PALSAR images because of misclassification in former and layover and shadow effects in latter. In table 6 and 7, the distribution of classes in different aspects is quite comparable as they are of the same sensor and same season. In northern aspects there is slight difference in PZ class due to variation in snow deposition patterns.

Table 8: Percentage area of classified zones in different elevations for RADARSAT-2 datasets

DEM (m)	Area(km^2)	PZ	IWPZ	IW	GIZ	DS	Debris
4161-4661	12.11	0	0	8.82	9.71	13.05	30.61
4661-5101	21.78	0	0	83.03	55.99	41.09	61.94
5101-5601	30.06	90.11	85.50	8.14	30.78	38.25	7.45
5601-6108	27.81	9.89	14.50	0	3.52	7.60	0

Table 9: Percentage area of classified zones in different elevations for 06-April-2009 ALOS/PALSAR datasets

DEM (m)	Area(km^2)	PZ	IWPZ	IW	GIZ	DS	Debris
4161-4661	12.11	0	0	0	0.27	23.30	47.45
4661-5101	21.78	5.02	0	77.02	76.52	44.85	52.55
5101-5601	30.06	89.44	87.01	22.31	22.15	29.65	0
5601-6108	27.81	5.54	12.99	0.66	1.07	2.20	0

Table 10: Percentage area of classified zones in different elevations for 06-April-2009 ALOS/PALSAR datasets

DEM (m)	Area(km^2)	PZ	IWPZ	IW	GIZ	DS	Debris
4161-4661	12.11	0	0	0	0.08	21.80	46.88
4661-5101	21.78	6.57	0	77.19	82.30	46.34	53.12
5101-5601	30.06	91.08	83.06	22.38	17.00	29.32	0
5601-6108	27.81	2.34	16.94	0.43	0.62	2.54	0

From tables 8, 9 and 10, we can state that the spatial distribution of classes PZ and IWPZ, with respect to altitude, shows that they are confined between altitudes ranging from 5101-6108 m. In these high altitudes very little melting is observed. A fraction of class IWPZ is also found at highest altitude i.e. 5601-6108 m and due to steep topography these ice walls are found in this region. After examining the damp snow areas in SVM classified outputs, also from table 8, 9 and 10 we can elucidate that damp snow areas at high altitude are mostly in southern aspects, these receive highest amount of solar radiations thus snow becomes damp even at high altitudes. Most part of the Class GIZ is limited in the elevation zone 4661-5107 m. Areas covered with debris are confined between 4161-5101 m elevation zones.

5.2 Velocity Estimation

5.2.1 SAR Interferometry

The ascending pass ERS- 1/2 SLC datasets were used for the process. A cartographic grid size of 25 m was used for further processing. Multilooking was performed with azimuth looks 6, range looks 1. A coherence threshold of 0.25 was used as threshold assuming small amount of displacement takes place along the glacier. Well distributed thirty five GCP'S were used in the process of refinement and reflattening. These refined unwrapped phase values were finally used to derive horizontal displacement. An interpolation window size of 3 with grid spacing of 25X25 m is used for geocoding and displacement mapping.

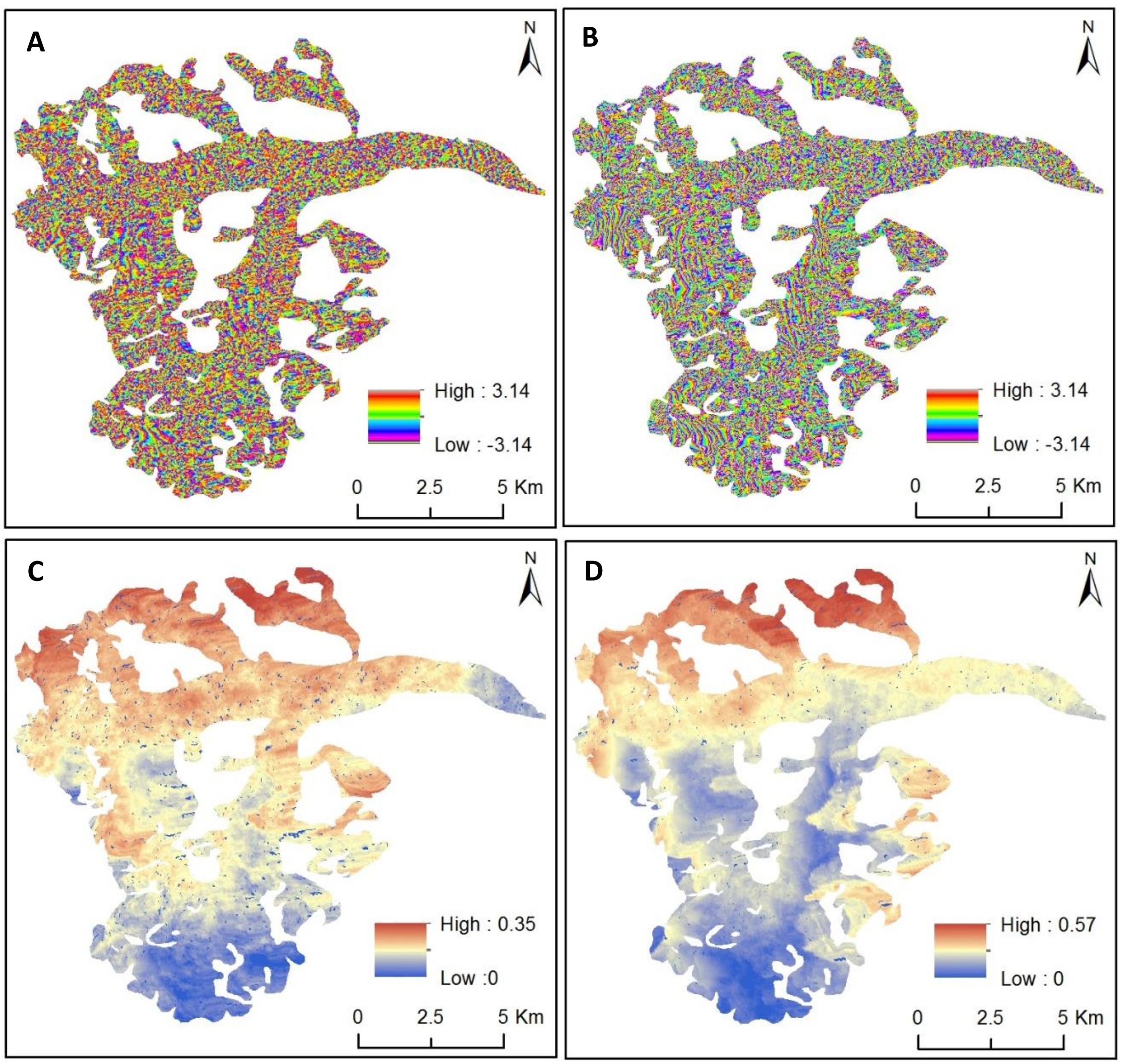

Figure 18: A) Interferogram for 28th-29th March-1996 B) Interferogram for 2nd-3rd May 1996 C) Displacement map for 28th-29th March-1996 D) Displacement map for 2nd-3rd May 1996

From the figure 18 (A and B) we can see differential fringes in the interferogram that indicate glacier movement occurs even for a small interval of one day. The density of fringes is more in figure 18 B which indicate higher displacement and can be seen from the figure 18 D. A mean displacement of 25.5 cm in the month of May and 18.2 cm in March suggests that glacier movement changes with seasonal variations. This can be due to the presence of excessive amount melt water at base in the month of May that decreases friction between glacial ice and bed rock causing enhanced basal flow. These ERS 1/2 images are acquired using ascending pass most part of the velocity component of this west-east flowing glacier lies in the satellite look direction this is the reason behind high rates of flow as seen in from the figure 18 (C and D). It can be clearly seen from the figure 18 (C and D) that glacier flow is not uniform and varies across the glacier; so there is need of studying displacement with variations in slope and aspect.

Table 11: Mean displacement for 28th-29th- March 1996 and 2nd-3rd May 1996 w.r.t. aspect

Aspect	Area (km^2)	Mean Displacement March(m)	Mean Displacement May(m)
Flat	46.5e-2	16.54e-2	22.10e-2
North	12.51	16.53e-2	22.44e-2
North-East	15.33	17.41e-2	23.74e-2
East	18.61	18.86e-2	25.99e-2
South-East	12.23	20.26e-2	28.84e-2
South	7.94	22.16e-2	32.92e-2
South-West	4.74	20.31e-2	30.25e-2
West	8.40	15.82e-2	21.36e-2
North-West	11.25	15.02e-2	20.87e-2

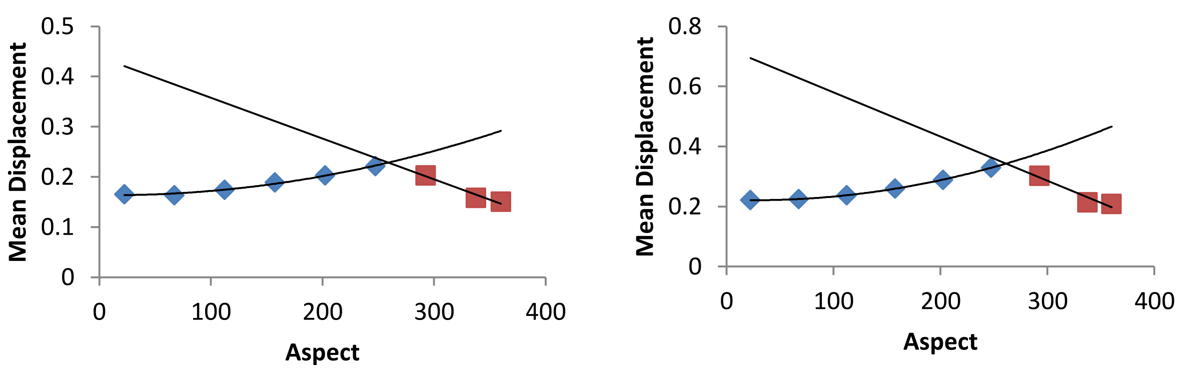

Figure 19: Mean displacement A) 28th-29th- March 1996 B) 2nd-3rd May 1996 w.r.t. aspect

The results listed in table 10 shows highest mean value of displacement is found in the southern aspects and lowest displacement rates are in northern aspects this is because of difference in the sun illumination. Southern aspects are more illuminated in Himalayan region in comparison to northern aspects. This difference in displacement values in both the aspects is more pronounced in for the month of May can be seen from the figure 19 B. The intersection point of two curves in both the figures represents highest displacement attained after this point the displacement values start to dip. The displacement values reach its maximum values with south-west aspect at an angle of 247.5 after this three is fall in the mean displacement values.

Table 12: Mean displacement for 28th-29th- March 1996 and 2nd-3rd May 1996 w.r.t. slope

Slope (Degree)	Area (km^2)	Mean Displacement March(m)	Mean Displacement May(m)
0-3	8.86	18.08e-2	22.64e-2
3-5	14.31	17.60e-2	23.08e-2
5-10	24.68	17.24e-2	23.99e-2
10-20	24.47	16.87e-2	24.25e-2
20-35	13.28	16.39e-2	24.38e-2
35-74	5.11	18.20e-2	26.62e-2

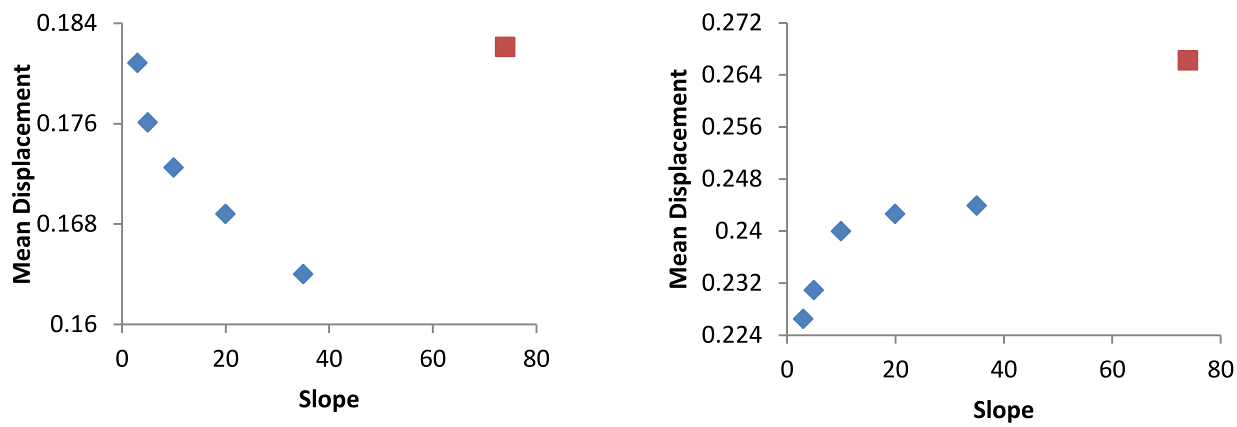

Figure 20: Mean displacement A) 28th-29th- March 1996 B) 2nd-3rd May 1996 w.r.t. slope

There is difference in the displacement patterns with respect to slope in both the datasets for different months. Figure 20 A. suggest that displacement values decreases for the slopes ranging from 10-35 degrees and then suddenly reaches its maximum at high slopes. A smooth increasing pattern is observed for the month of May as can be seen from the figure 20 B. The reason for these low flow rates at high slopes in month of March can be due the variation in temperature, as temperature is below freezing point at this time of the year at high altitudes bed rock is frozen therefore less amount of melt water is produced at the base, only internal deformation occurs. However at low altitudes ice flows is due to internal deformation and also enhanced basal flow occurs due to the presence of melt water at the base. Figure 20 B shows an increasing pattern of flow with the increase in slope for the month of May, temperature at this time of year is comparatively high so enough melt water is produced, even at high altitudes leading to a larger amount of basal flow. In high sloppy terrain extraordinary rates are found these because of the profound effect of slope on the movement of the glacier can be seen as red points in the figures 20 A, B. Due to these extraordinary high rates at high slopes these points are off the curve and therefore excluded from the spatial analysis.

Using the results from the figure 20 A, B we can model the blue points in both the figure as exponential curves. Figure 20 A can be modeled using the equation:

$$y = a + b * e^{(-c \times slope)} \tag{30}$$

In figure 20 B the graph is going up thus the first five blue points can be modeled using the equation:

$$y = a + b * (1 - e^{(-c \times slope)}) \tag{31}$$

Here, $a =$ lowest value for the mean displacement,
$b =$ average difference between the mean displacement of two successive points,
$c =$ rate of change of mean displacement w.r.t. slope also this constant has directional constituent.

The regression analysis is done using R statistical software using the Non-linear least square estimates.

Table 13: Regression analysis summary for mean displacement w.r.t. slope for the month of March

Regression Summary	a	b	c
	0.163038	.020966	.075697
Residual Standard Error		0.001521	
Degree of Freedom		2	
Number of Iterations		8	
Formula		$y \sim a + b * e^{(-c \times slope)}$	

Table 14: Regression analysis summary for mean displacement w.r.t. slope for the month of May

Regression Summary	a	b	c
	0.212300	.031440	.192580
Residual Standard Error		0.000943	
Degree of Freedom		2	
Number of Iterations		6	
Formula		$y \sim a + b * (1 - e^{(-c \times slope)})$	

Table 15: Estimated and true value of mean displacement for the month of March and May

Slope (Degree)	Mean Displacement March (m)		Mean Displacement May (m)	
	True value	Estimated Value	True value	Estimated Value
0-3	18.08e-2	16.52e-2	22.64e-2	22.60e-2
3-5	17.60e-2	16.35e-2	23.08e-2	23.17e-2
5-10	17.24e-2	16.30e-2	23.99e-2	23.91e-2
10-20	16.87e-2	16.30e-2	24.25e-2	24.30e-2
20-35	16.39e-2	16.30e-2	24.38e-2	24.37e-2

The estimated values for the month of May are much accurate than the values estimated for the month of March.

5.2.2 Feature Tracking

5.2.2.1 SAR Data

Although interferometry can be used to detect surface variations with high level of accuracy; it suffers due to phase decorelation. Snowfall, melting of snow and rapid movement are some of the reasons for decorelation. The displacement maps derived using SAR interferometry are just the representation of few days thus cannot be generalized. Feature tracking is an alternative approach and can be used to monitor glacier kinematics for both long term and short term basis. SARscape module which runs under ENVI is used for feature tracking. Offset tracking can be implemented in two ways coherence feature tracking and amplitude feature tracking. Coherence tracking is much more accurate but has a limitation of dependency on the phase information like InSAR technique; it works well on areas with high coherence values but fails in glaciers where coherence is generally low and this technique has high computational cost.

Amplitude tracking estimates the glacier displacement by means of intensity. The data sets required are two pairs of SLC images where pre-event acts as master and post-event acts as slave. This approach can be divided into two major steps; coregistration and cross-correlation. Coregistration is done to superimpose images at sub-pixel level accuracy. Different coregistration settings are used; best setting is obtained from the mean values with small standard deviation. After this process of coregistration the shift between the images can be estimated. The parameter settings used for amplitude tracking should be decided carefully if the look rate in low and the size of window is large then the results are dominated by pattern like structure(Neelmeijer, 2012). The number of looks should be five times the settings used for multilooking(SARscape 2010). The window size should be chosen to accommodate largest possible displacement. The data is oversampled to increase the accuracy. The success of offset tracking depends on the similar and distinguishable characteristics in the intensity data that can be located within the same compared image patch(Strozzi et al., 2002).

The process yields three output images; first one is the cross-correlation image having values ranging from 0 to 1. The other two images are range and azimuth shift in pixel units. These images are transformed into metric units by multiplying with actual pixel spacing which is given in the corresponding header file. After transforming these images into metric units geocoding has to be done. The geocoded map is outliered for the identification of the erroneous values; these values are then labeled as NaN. In this study the outliers are identified using the mean and the standard deviation by the equation (29)

$$\mu \pm 3\sigma \qquad (29)$$

This outlier equation adopted is large enough to accommodate all the realistic motion of pixels and rest are discarded and labelled as NaN.

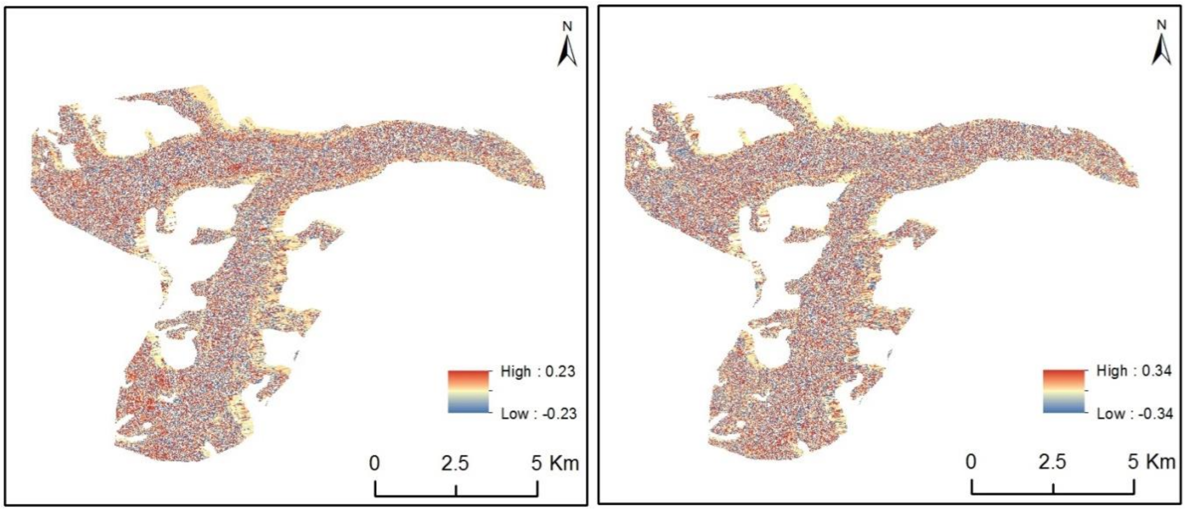

Figure 21: Feature tracking results for pair 25th-September-2013 to 28th-October-2013 using TanDEM-X datasets A) Velocities per day in range direction negative values point direction towards east B) Velocities per day in azimuth direction negative values indicate movement toward south

Figure 21 shows velocity patterns in range and azimuth direction. For the estimation of velocities using feature tracking technique a subsetted portion of the glacier is considered as feature tracking can be done with identifiable features. The temporal variation of 33 days in the TanDEM-X pair cannot be used for InSAR due to large temporal variation there is loss of coherence between the image pairs. An oversampling rate of 16 was used for the process of amplitude tracking this means that a theoretical precision 1/16 of the pixel spacing can be achieved. Images from different seasons and sensors were used for amplitude tracking.

Table 16: SAR datasets amplitude tracking results

Satellite	Selected Image Pair	Velocity day^{-1}		Pixel Spacing	
		Azimuth (cm)	Range (cm)	Azimuth (m)	Range (m)
ALOS/PALSAR	13/09/2009 – 1/08/2010	7.5	6.0	9.36	9.36
RISAT-1	15/04/2013 – 1/11/2013	8.7	7.1	7.19	7.19
TanDEM-X	25/09/2013 – 28/10/2013	13.1	8.9	1.98	1.36

From the table 16 we can state that the velocity of the glacier varies with season. The ALOS/PALSAR datasets are covering about whole year so the velocity values are representing the whole year, covering the winter as well as the summer season thus they are representing the average velocity for almost a year and low rate of flow i.e. 7.5 cm/day in azimuth and 6.0 cm/day in range are seen these are less in comparison to other results listed in table 16. RISAT-1 datasets are covering seasons from early summer to the late summer as most part of the glacier is melting at this time velocities of 8.7 cm/day in azimuth and 7.1 cm/day in range are seen these are higher in comparison to ALOS/PALSAR datasets. TanDEM-X data sets are representing only a short time period of end of ablation season thus relatively high rates of flow of 13.1 cm/day in azimuth and 8.9 cm/day in range are noticed. As the precision depends on the pixel spacing using the values of table 13 we can say that velocity estimates using TanDEM-X data sets are the most accurate. The expected error is 8.5 cm in range direction with pixel spacing of 1.36 m. Azimuth image is less accurate with a precision 12.3 cm due to a pixel spacing of 1.98 m.

5.2.2.2 Optical Images

Optical images used for feature tracking must be coregistered and orthorectified so that measurements using these images are in scale. Images having minimum snow cover are selected for this study so that features are clearly visible. Region of interest i.e. study area is masked out from the images to reduce the computational time. After these steps of preprocessing glacier displacement using feature tracking is carried out. Cosi-Corr, a module which runs under ENVI has been used for feature tracking. For implementing this technique two images are required, one pre-event and other post-event. Maximum value of cross-correlation is deduced in the two images and relative displacement is estimated. In Cosi-Corr two options for correlation are available; frequential and statistical. Frequential is fourier based and displacement is retrieved from the relative phase difference between the two images(Leprince et al., 2007). The parameters like window size, step, robustness, iterations and mask threshold used in frequency correlator have to be carefully selected to obtain an optimal displacement value. An initial window size of 64 and final window size of 16 is used with step of 2 pixels and robustness of four pixels(Leprince, 2013). Once the displacement values are estimated outliers are identified in the same way as done for microwave datasets.

Table 17: Feature tracking results for optical images

Satellite	Time Interval	Selected Image Pair	Velocity day^{-1}	
	Days		NS (cm)	EW (cm)
Landsat-7 ETM	415	09/07/1999 – 28/08/2000	7.7	9.3
Landsat-7 ETM	304	28/08/2000 – 28/06/2001	9.4	9.7
Landsat-7 ETM	400	28/06/2001 – 02/08/2002	9.4	10.0
Landsat-8 OLI/TIRS	384	23/07/2013 – 11/08/2014	5.5	6.2
Aster	752	08/09/2004 – 30/09/2006	7.0	7.8

From the results of the above table we can see the feature tracking results for optical images. The pairs are mostly having a temporal difference of almost a year with Aster image pair having difference of two years in acquisition. The values in the table 17 are thus representing yearly glacier velocity. Using the results from above table average velocities of 7.8 cm/day is found in north-south direction and 8.6 cm/day in East-west direction. There is slight difference in the velocity values due to the variation in the snow cover, feature tracking results vary with the variations in the snow cover. In some cases the algorithm is not able to detect the identifiable features due to the presence of snow.

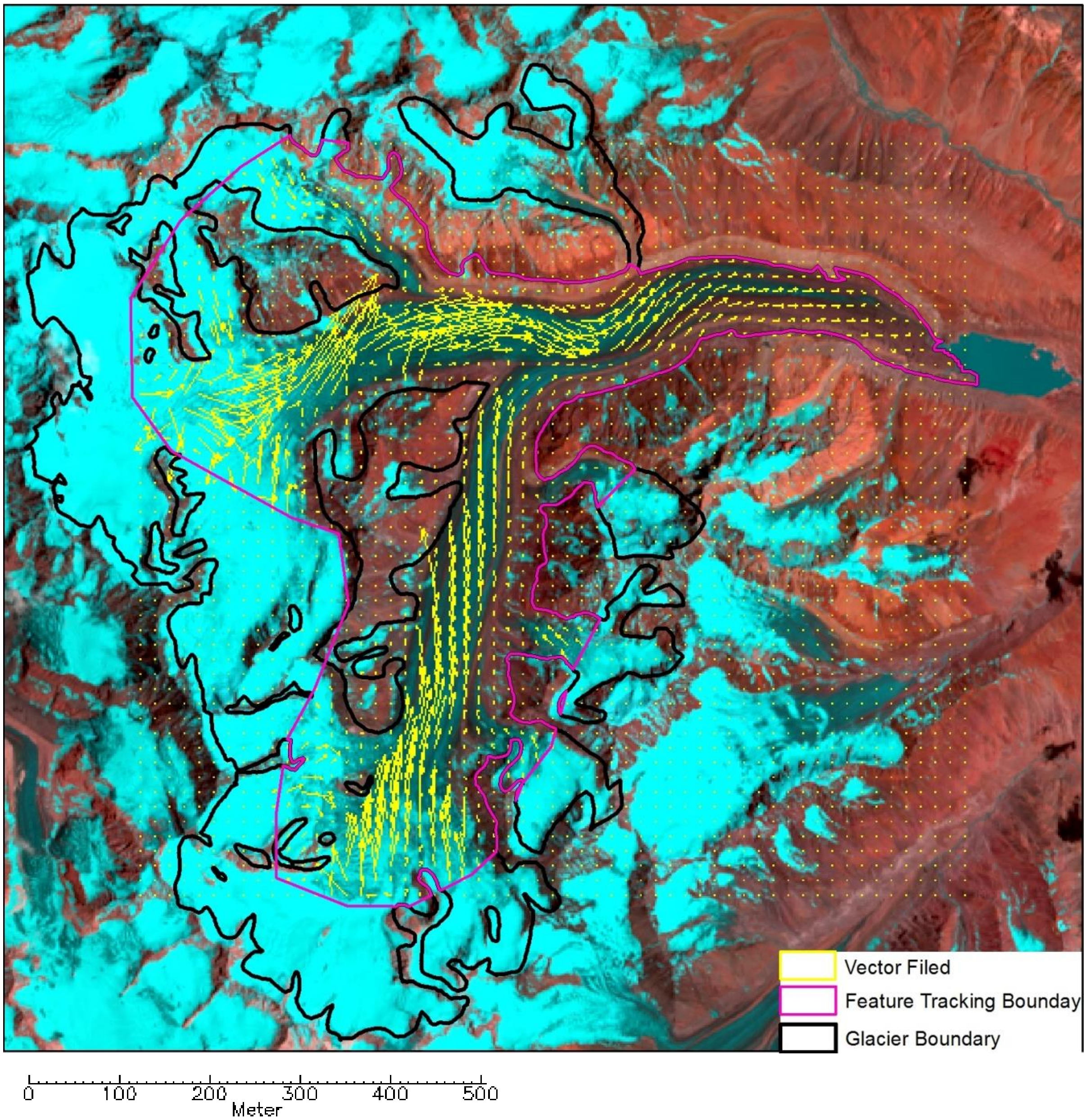

Figure 22: Vector field overlaid on Samudra Tapu glacier FCC

Figure 22 shows the vector field for the glacier with yellow color; length of the arrow represents the magnitude flow. It can be inferred from the figure that glacier flow is greater at high altitudes and decreases near the snout this flow pattern is in accordance with the figure 18, the InSAR derived velocity estimates. The pink boundary shown in the figure 22 represents the portion of the glacier used for feature tracking. Only some part of the ablation area is considered for feature tracking as this technique is based on identifying features and mapping their displacement. Most of the identifiable features such as crevasses are found in ablation areas and besides patterns of ice walls can also be tracked.

5.3 Rate of Flow for Classified Zones

In this research glacier is classified into various zones and the velocity was estimated for the glacier so this section correlation of both these results is done and the rate of flow various classified zones is analyzed. Images with different seasons and spatial resolution were used for the purpose of classification and also images with different spatial resolution were used for the velocity estimates. Datasets used for correlation are chosen with a certain level of similarity primarily in terms of spatial resolution.

Table 18: Rate of flow for different classes for 12-Apr-2009 classified results and 28^{th}-29^{th}-March-1996 InSAR displacement results

Class	Maximum (m)	Mean (m)	Standard Deviation (m)
DS	34.71e-2	19.55e-2	5.2e-2
Debris	29.11e-2	19.20e-2	3.8e-2
IW	33.65e-2	19.09e-2	5.2e-2
IWPZ	35.58e-2	17.78e-2	6.6e-2
PZ	35.29e-2	16.86e-2	6.8e-2
GIZ	34.29e-2	16.87e-2	4.8e-2

Table 19: Rate of flow for different classes for 12-Apr-2009 classified results and 2^{nd}-3^{rd}-May- 1996 InSAR displacement results

Class	Maximum (m)	Mean (m)	Standard Deviation (m)
DS	56.98e-2	26.39e-2	8.5e-2
Debris	47.60e-2	25.50e-2	5.3e-2
IW	54.73e-2	26.43e-2	8.6e-2
IWPZ	57.30e-2	25.82e-2	10.4e-2
PZ	54.83e-2	23.34e-2	11.2e-2
GIZ	52.04e-2	21.68e-2	8.4e-2

From the tables 15, 16 we can see highest rate of flow for the class IWPZ as these are found at high altitude slope thus are moving fast. Lowest flow rates are seen for debris covered areas, these found near the snout, glacier moves slowest in these regions. High values of standard deviations are seen for the regions with percolation zone this is because of the variation of the distribution of class PZ which is found both in areas with low slope and high sloppy terrain. GIZ class has minimum flow rate as most of it is sited at low slope areas. The mean values of flow for class PZ and IWPZ which form the accumulation area are relatively lower than other classes which form the ablation area this clearly suggests that accumulation areas are moving slowly than other parts of the glacier. From the tables 15, 16 we can conclude that the entire glacier is moving faster in the month of May in comparison to March. The reason behind this can this high rate of flow may be due to the excessive melting of snow in the month of May, which can cause change in the phase values from the same area thus leading to high rates of flow.

6. DISCUSSIONS

This chapter discusses the results presented in the results section obtained from the proposed methodology discussed in the methodology section.

6.1 Glacier Classification

For the purpose of identification of distinct zones of the glacier two techniques were used a) Multi-temporal analysis b) Polarimetric decompositions. Multitemporal analysis uses three images of different seasons and on the basis of varying backscatter characteristics zones were identified. Images used for the polarimetric decompositions were of winter and early summer, during these seasons the glacier is covered with seasonal snow which is dry at the surface and due to microwave penetration underneath subsurface features can be identified. SVM’s were used for the final classification. The derived classes can be articulated as accumulation and ablation areas thus these zones can be mapped. The accumulation and the ablation regions can be derived from the classified results using the figure 1.

Table 20: Accumulation and ablation areas in km^2 using different SAR datasets

Datasets	Accumulation Area	Ablation Area
RISAT-1 (Multi-Temporal)	48.06	38.83
RADARSAT-2 (27-01-2014)	35.22	54.04
ALOS/PALSAR (06-04-2009)	33.12	37.5
ALOS/PALSAR (12-04-2011)	33.16	38.03

The areal extent of accumulation area from the above table is quite comparable but very high values for the accumulation region is seen for RISAT-1 datasets this can be because damp snow was not included as a class in RISAT-1 classified outputs. Damp snow can be found at high altitudes of the accumulation areas and also in ablation areas. The class damp snow was included in ablation area thus there is difference in results. The extent of ablation area is low in ALOS/PALSAR datasets because some portion of ablation area was removed as layover and shadow.

The boundary separating accumulation zone and ablation zone referred as ELA, and is determined at an altitude of about 5200m (MSL) for this glacier. This altitude line is in accordance to a study by Kulkarni which quantifies snow line at the end of ablation season, at approximately 5200 m(Kulkarni, 2007). ELA is equal to snow line at the end of ablation season as there is no superimposed ice zone in temperate glaciers, at this point net accumulation is equal to net ablation this altitude is very important for mass balance studies. ELA was determined from the classified outputs and optical images were also used as an additional reference. The lowest point at which damp snow is present is found at an altitude of 4335m (MSL). This point was also identified using a hand held GPS during the filed visit at an altitude of 4330m (MSL). The estimated vertical accuracy is of 20 m for ASTER GDEM thus the determined altitude lines have this intrinsic error(Japan Space Syatems, 2012).

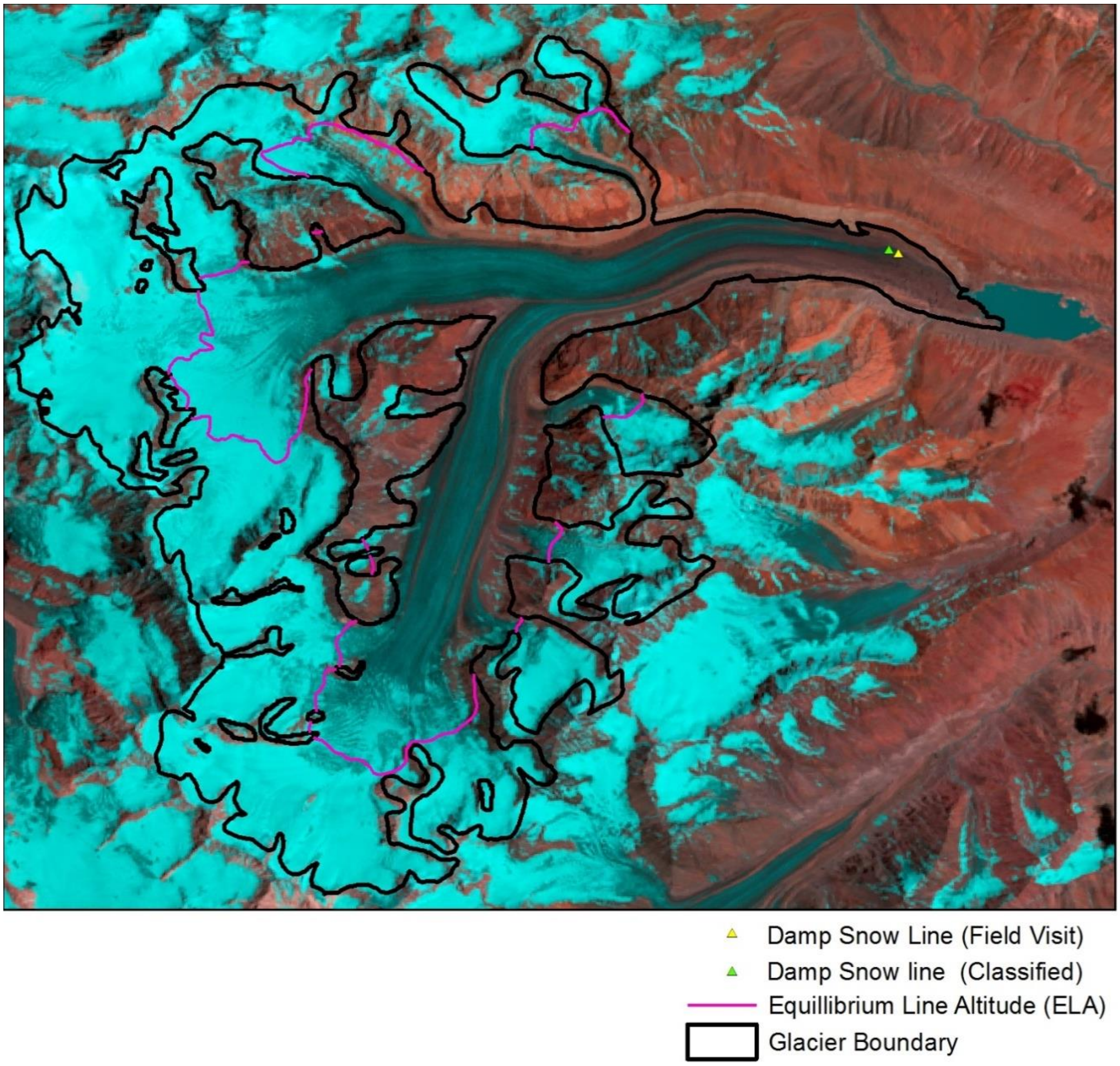

Figure 23: ELA separating accumulation and ablation areas for Samudra Tapu glacier

6.2 Velocity Estimation

SAR interferometry and offset feature tracking techniques were used for the velocity estimates.

SAR interferometric techniques are highly accurate and can be used to retrieve glacier velocities. After the effect of topography is removed from the interferogram the fringes represent horizontal and vertical displacement. Figure 18 clearly suggest that fringes of the interferogram represent horizontal displacement. Several assumptions are considered using InSAR velocity estimates one of the most important is that the change in surface elevation between the two SAR acquisitions is negligible. The velocity estimates are only calculated towards the satellite view direction thus the displacement towards the LOS of the radar viewing angle is calculated.

InSAR technique depends on the coherence and also there is limited number of available scenes, feature tracking is an alternative approach for monitoring glacier velocity both in long term and shot term perspectives. In this study feature tracking was done for SAR as well as optical data sets. Feature tracking is not as accurate as InSAR and errors due to misregistration and orthorectification propagate in the final velocity estimates. Furthermore only identifiable features can be tracked using this approach most of them are found in the ablation region and velocity estimates cannot be considered as a representation of the whole glacier.

Table 21: Mean displacement for Samudra Tapu glacier obtained using different sensors

Selected Image Pairs	Satellite	Displacement Day^{-1}	
		Azimuth (cm)	Range (cm)
28th - 29th March 1996	ERS 1/2	-	18.2
2nd – 3rd May 1996	ERS 1/2	-	25.5
13/09/2009 – 1/08/2010	ALOS/PALSAR	6.0	7.5
15/04/2013 – 1/11/2013	RISAT-1	8.7	7.1
25/09/2013 – 28/10/2013	TanDEM-X	13.1	8.9
		N-S (cm)	E-W (cm)
09/07/1999 – 28/08/2000	Landsat-7 ETM	7.7	9.3
28/08/2000 – 28/06/2001	Landsat-7 ETM	9.4	9.7
28/06/2001 – 02/08/2002	Landsat-7 ETM	9.4	10.0
23/07/2013 – 11/08/2014	Landsat-8 OLI/TIRS	5.5	6.2
08/09/2004 – 30/09/2006	Aster	7.0	7.8

Velocity estimates for Samudra Tapu glacier are listed in the above table show different velocity rates that occur at different time periods. As per the literature InSAR velocity estimates are highly accurate and they represent the whole glacier. The limitation of these results is that they represent a short time period and the results can be affected by melting of snow, snowfall and high speed wind can also change the patterns of snow all these listed factors can lead to phase change and induce errors in the obtained velocity patterns. Using InSAR derived results a mean displacement values of 18.2 cm/day for the month of March and 25.5 cm/day in the month of May are noticed. These values are higher than the results derived from feature tracking; this is due to the non-inclusion of a northern branch and upper accumulation areas of the glacier in feature tracking. These regions are having substantial slopes and high rates of flow are found in these regions.

Analysis of the velocity patterns with respect to slope show that increasing trend of velocity is seen with increase in slope these results become more profound in summers when glacier is melting. Relatively higher rates of flow are seen in southern aspects. These results show that glacier flow is affected by terrain parameters. This spatial analysis was not carried out for the results acquired from feature tracking as a subsetted part of the glacier was used for offset feature tracking. This region of interest had only some classes of slope with substantial amount of area and mainly two aspects were i.e. east and north aspects were dominating in this subsetted portion. If we use merge different classes slope and aspect to increase area then it leads to a very less number of points to plot and it’s difficult to find a trend among them.

The error of obtained feature tracking results can be quantified from pixel spacing, coregistration failures and orthorectification accuracy. Failure of image cross correlation can occur in small patches and thus can be considered as random error. Different rates of flow are seen using feature tracking of SAR datasets; this is due to the difference in time period of the used data this clearly depicts that glacier flow varies with season. The optical images used in this study are those which are having minimum snow cover so that feature can be easily tracked also these pairs are having a temporal difference of almost a year. An average flow rate of 7.8 cm/day in north-west direction and 8.6 cm/day in east-west direction is derived using these image pairs. These values represent glacier velocity of the whole year.

Table 22: Errors in datasets used for feature tracking

Datasets	Error	
	Azimuth	Range
ALOS/PALSAR	58.55 cm	58.55 cm
RISAT-1	44.94 cm	44.94 cm
TanDEM-X	12.3 cm	8.5 cm
	N-S	E-W
Landsat-7	7.3 m	7.3 m
Landsat-8	6 m	6 m
ASTER	6 m	6 m

The results from table 22 clearly suggest that SAR datasets have less error in comparison to optical datasets. TanDEM- X datasets are found to be the most accurate. An error of 7.3 m is found in landsat-7 datasets(NASA, 2011). Landsat-8 and ASTER data sets have an error of 6 m, ASTER datasets were orthorectified using Landsat-8 data so they have similar error(U S Geological Survey, 2014).

Ideally, ground measurements can be used for the validation of the obtained velocity patterns but these were not available for this study. Quantification of error in these derived velocity patterns can be done using the in-situ measurements.

6.3 Rate of Flow for Classified Zones

Flow rates of different classified zones are analyzed. The spatial resolution of the images used for the classification and the datasets used for velocity estimates must be comparable. Hence ERS-1/2 datasets and L-band ALSO/PALSAR datasets both having the spatial resolution of 25m were used for this study. Furthermore the results produced by the feature tracking of SAR and optical data are only representation of the ablation area and cannot be used for this analysis. The results from tables 15, 16 indicate that relatively low rates of flow are noticed for classes PZ and IWPZ which together form the accumulation area and higher rates of flow are seen for other zones which form the ablation areas. Hence we can say that the flow rate for the different zones of the glacier varies. This variation of flow rate is because of the difference in the amount of the melt water produced at high altitudes is less thus there is limited amount of basal flow.

7. CONCLUSIONS AND RECOMMENDATION

In this present study, glacier was classified into different zones, hence accumulation and ablation areas were mapped also the equilibrium line altitude and snow line altitude at the end of ablation season was determined. In this study velocity of the glacier using SAR interferometry and offset feature tracking using SAR and optical images was done. These techniques helped in monitoring glacier flow in both long term and seasonal perspectives. This study quantified the effect of terrain parameters like slope and aspect on the movement of the glacier. Finally the rate of flow of different classified zones was studied. The extents of the accumulation and ablation area, also the rate at which these are flowing are the most important factors in determining the life of a glacier.

7.1 How useful is Polarimetric SAR (PolSAR) for identifying different glacier facies?

Scattering mechanism varies in different zones of a glacier. Dry snow found at high altitude exhibits volume scattering. Ice walls being a corner reflector show double bounce scattering mechanism. In ablation areas at high altitude glacial ice acts as specular reflector and has a high component of surface scattering. Debris covered areas show both double bounce and surface scattering mechanism. Fully polarimetric data having HH, HV, VH, VV polarizations collectively form the scattering matrix. This scattering matrix can be decomposed using several decomposition techniques and different types of scatters i.e. volume, surface and double bounce scattering can be identified thus the type of snow pack can be determined. Referring to section 5.1.4 table 4 all the listed zones were identified using polarimetric decompositions, ice walls were divided into two parts using the DEM.

7.2 How to map the accumulation and ablation areas for a glacier?

Accumulation areas of the glacier are the regions where snow is accumulating and adding to the glacier mass. Further down the glacier, at a lower altitude is the ablation area where ice mass is lost due to melting. These areas are separated by ELA, the altitude where net accumulation is equal to net ablation. By classifying the glacier into different zones we can identify the regions of percolation zone, glacial ice and debris. As percolation zone is the zone where little melting takes place in late summers and winter accumulated snow is not completely melted, these form the accumulation areas of the glacier in these regions ice mass is increasing. The regions of glacial ice and debris are the zones where melting takes place and form the ablation areas of the glacier. ELA which divides accumulation and ablation area was found at an altitude of 5200 m above MSL. During the field visit the debris covered region was seen as little elevated in comparison to the regions with ice this is because the debris insulates the underneath ice and melting takes place at lower rate.

7.3 What is the analysis of accuracy, robustness and efficiency of SVM?

SVM's are better than other classification methods in terms of recognition and misrecognition rate and thus are more accurate(Camps-valls et al., 2004). An additional advantage of using SVM is that it minimizes the classification error i.e. the probability of misclassification is minimum. SVM's are computationally fast in comparison to statistical approaches like maximum likelihood (ML) and Artificial Neural Networks (ANN)(Tso et al., 2009). Noisy bands and outliers are the unwanted data which can lead to loss of generalization. SVM's are robust to outliers and are more stable(Camps-valls et al., 2004).
From section 5.1.4 table 4 we can see that high values of classification accuracy and Kappa coefficient were retrieved using SVM's.

7.4 How can Interferometric SAR (InSAR) be used to estimate glacier displacement?

Using SAR interferometry to determine the glacier velocity was discovered by R.M. Goldstein by using ERS data sets. Two radar images acquired for the same area using similar geometry from different orbits which are separate by a small distance. The phase of single acquisition is of no use but the phase difference of both these images result in an interferogram, whose phase contains differences in range and topographic effects. Once topographic effects are removed the resultant interferogram contains only the phase due to displacement in the range direction. Subtracting the phase of two images leads to 2π ambiguity, which means that a phase difference of $3\pi/2$ is represented as $\pi/2$. The process of removing this uncertainty is called phase unwrapping. The orbits of the satellite are then to be refined using a GCP file and finally this refined phase is converted to displacement. ERS 1/2 datasets which were used in this study had a temporal difference of one day, due to this high value of coherence can be retained and interferometry is possible. Mean displacements of 18.2 cm/day for the month of March and 25.5 cm/day in the month of May were noticed using InSAR technique.

7.5 What is the accuracy of the estimated glacier displacement obtained from InSAR and offset feature tracking of SAR and optical datasets?

SAR interferometry can detect centimeter scale distortions on earth's surface(Reigber et al., 2003). Offset feature tracking error propagates due to misregistration and orthorectification and the expected accuracy is of $1/10^{th}$ of the pixel size which is far less than the accuracy of SAR interferometry. Also the presence of snow makes features less visible and hence they are difficult to track this leads to erroneous values in the displacement. Although InSAR is much more accurate, it has limitations of loss of coherence which can occur due to large temporal difference, rapid surging of the glaciers and climatic conditions like snowfall and melting of snow. Furthermore the results are just the representation of few days and thus cannot be generalized. Using offset feature tracking glacier velocity can be monitored for seasonal and long term basis.

7.6 What are the effects of terrain parameters and climatic conditions on the movement of the glacier?

Slope, a terrain parameter certainly has an effect on the movement of the glacier generally an increasing pattern of glacial flow is seen with the increase in the slope. But due to less amount of melt water produced at high altitudes there is little reduction in glacial flow even at high slopes this phenomenon is pronounced at the time of winter. Climatic conditions such as sun illumination certainly effect the movement of the glacier and high rates of flow are seen in the southern aspects as these are more sun illuminated thus surplus melt water is produced at the base causing enhanced basal flow.

7.7 Recommendations

Followed by this research some of the recommendations are discussed below.

- This study uses quad-polarization data sets for polarimetric decompositions but these datasets have coarser resolution and less number of data takes. Polarimetric analysis using HH-VV can also be performed which will have more number of data sets to work on and also at fine resolution.

- Use of TanDEM-X along track interferometry to observe glacier mass change using large baseline can help in mapping the accumulation and ablation areas and also help in mass balance studies

- This study is limited to a two dimensional glacier flow, using both ascending and descending passes three dimensional glacier displacements can be estimated using InSAR technique.

- Validation of obtained glacier flow using remote sensing techniques like InSAR and offset feature tracking with in-situ measurements will help to monitor glacier movement in impeccable configuration.

- Applying a directional filter on the results obtained from offset feature tracking manually defining a direction for glacier flow and discard displacement vectors that deviate from this priori direction of flow.

- Studying retreat or advance of the glacier with respect to its snout and the displacement can provide better perspective about the glacier.

- Most important is the vertical profiling of the glacier obtained from Ground Penetrating Radar (GPR) which can provide us the details of the bed rock and understand internal properties of glacier.

BIBLIOGRAPHY

Ahmad, S., Hasnain, S. I., & Selvan, M. T. (2004). Morpho-metric characteristics of glaciers in the Indian Himalayas. *Asian Journal of Water, Environment and Pollution 1*(1), 109–118.

Aizen, V. B., Kuzmichenok, V. A., Surazakov, A. B., & Aizen, E. M. (2007). Glacier changes in the Tien Shan as determined from topographic and remotely sensed data. *Global and Planetary Change 56*, 328–340. doi:10.1016/j.gloplacha.2006.07.016

Anukesh, K. A. (2013). Gangotri glacier motion studies using SAR based InSAR and feature tracking techniques. *University of Twente.*

B.Tso, & P.Mather. (2009). Classifiation meathods for remotely sensed data. (S. Edition, Ed.). *CRC Press Taylor and Francis Group*.

Berthier, E., Arnaud, Y., Kumar, R., Ahmad, S., Wagnon, P., & Chevallier, P. (2007). Remote sensing estimates of glacier mass balances in the Himachal Pradesh (Western Himalaya , India). *Remote Sensing of Environment 108*, 327–338. doi:10.1016/j.rse.2006.11.017

Berthier, E., Vadon, H., Baratoux, D., Arnaud, Y., Vincent, C., Feigl, K. L., … Legrésy, B. (2005). Surface motion of mountain glaciers derived from satellite optical imagery. *Remote Sensing of Environment*, *95*(1), 14–28. doi:10.1016/j.rse.2004.11.005

Bhattacharya, A., Arora, M. K., & Sharma, M. L. (2012). Usefulness of synthetic aperture radar (SAR) interferometry for digital elevation model (DEM) generation and estimation of land surface displacement in Jharia coal field area. *Geocarto International*, *27*(1), 57–77. doi:10.1080/10106049.2011.614358

Bindschadler, R. A., Jezek, K. C., & Crawford, J. (1987). Glaciological investigations using synthetic aperture radar systems. *Annals of Glaciology*, *9*.

Bolch, T., Pieczonka, T., & Benn, D. I. (2011). Multi-decadal mass loss of glaciers in the Everest area (Nepal Himalaya) derived from stereo imagery. *The Cryosphere*, *5*(2), 349–358. doi:10.5194/tc-5-349-2011

Brown, L. G. (1992). A Survey of Image Registration. *ACM Computer Survey*, *24*(4), 325–376.

Camps-valls, G., Gómez-chova, L., Calpe-maravilla, J., Martín-guerrero, J. D., Soria-olivas, E., Alonso-chordá, L., & Moreno, J. (2004). Robust Support Vector Method for Hyperspectral Data Classification and Knowledge Discovery. *IEEE TRANSACTIONS ON GEOSCIENCE AND REMOTE SENSING*, *42*(7), 1530–1542.

Cloude, S. R., & Pottier, E. (1996). A review of target decomposition theorems in radar polarimetry. *IEEE TRANSACTIONS ON GEOSCIENCE AND REMOTE SENSING*, *34*(2).

Cloude, S. R., & Pottier, E. (1997). An Entropy Based Classification Scheme for Land Applications of Polarimetric SAR. *IEEE TRANSACTIONS ON GEOSCIENCE AND REMOTE SENSING 35*(1), 68–78.

Dhar, S., Kulkarni, A. V, Rathore, B. P., & Kalia, R. (2010). Reconstruction of the moraine dammed lake , based on field evidences and paleohistory , Samudra Tapu Glacier , Chandra Basin, Himachal Pradesh. *Indian Society of Remote Sensing*, *38*(March).

Dixit, A., & Agarwal, S. (2013). Comparison of various models and optimum range of its parameters used in SVM classification of digital satellite image. *2013 IEEE Second International Conference on Image Information Processing (ICIIP-2013)*, 363–368. doi:10.1109/ICIIP.2013.6707616

Eriksson, M., Jianchu, X., Shrestha, A. B., Vaidya, R. A., Nepal, S., & Sandström, K. The changing Himalayas – Impact of climate change on water resources and livelyhoods in the greater Himalaya. *ICIMOD*.

Evans, A. N. (2000). Glacier surface motion computation from digital image sequences. *IEEE TRANSACTIONS ON GEOSCIENCE AND REMOTE SENSING 38*(2), 1064–1072.

La Frenierre, J., & Hamann, H. (2009). Measuring the mass balance of mountain glaciers: A review of techniques and recent investigations.

Floricioiu, D. (2011). TerraSAR-X and TanDEM-X satellite missions update, 13–14.

Frey, H., Paul, F., & Strozzi, T. (2012). Compilation of a glacier inventory for the western Himalayas from satellite data: methods, challenges, and results. *Remote Sensing of Environment*, *124*, 832–843. doi:10.1016/j.rse.2012.06.020

Funk, M. (2013). Physics of glaciers I 651-4101-00 /, (June 2006).

Gao, J., & Liu, Y. (2001). Applications of remote sensing , GIS and GPS in glaciology : a review, *4*, 520–540.

Giles, a. B., Massom, R. a., & Warner, R. C. (2009). A method for sub-pixel scale feature-tracking using Radarsat images applied to the Mertz Glacier Tongue, East Antarctica. *Remote Sensing of Environment*, *113*(8), 1691–1699. doi:10.1016/j.rse.2009.03.015

Gourmelen, N., Kim, S. W., Shepherd, a., Park, J. W., Sundal, a. V., Björnsson, H., & Pálsson, F. (2011). Ice velocity determined using conventional and multiple-aperture InSAR. *Earth and Planetary Science Letters*, *307*(1-2), 156–160. doi:10.1016/j.epsl.2011.04.026

GSI. (n.d.). Geological Survey of India GSI,Ministry of Mines,Government of India - Indian Geology - Glacier. Retrieved from http://www.portal.gsi.gov.in/portal/page?_pageid=127,711653&_dad=portal&_schema=PORTAL

Gupta, R. P., Haritashya, U. K., & Singh, P. (2005). Mapping dry/wet snow cover in the Indian Himalayas using IRS multispectral imagery. *Remote Sensing of Environment*, *97*(4), 458–469. doi:10.1016/j.rse.2005.05.010

Hagen, J. O., Reeh, N., Hagen, J. O., & Reeh., N. (2004). *<i>In situ</i>*

measurement techniques: land ice

Haughton, J. T., & Ding, Y. (2001). *CLIMATE CHANGE IPCC REPORT 2001*.

Heid, T., & Kääb, A. (2012). Evaluation of existing image matching methods for deriving glacier surface displacements globally from optical satellite imagery. *Remote Sensing of Environment*, *118*, 339–355. doi:10.1016/j.rse.2011.11.024

Huang, L., & Li, Z. (2011). Comparison of SAR and optical data in deriving glacier velocity with feature tracking. *International Journal of Remote Sensing*, *32*(10), 2681–2698. doi:10.1080/01431161003720395

Huang, L., Li, Z., Tian, B.-S., Chen, Q., Liu, J.-L., & Zhang, R. (2011). Classification and snow line detection for glacial areas using the polarimetric SAR image. *Remote Sensing of Environment*, *115*(7), 1721–1732. doi:10.1016/j.rse.2011.03.004

Jaenicke, J., Mayer, C., Scharrer, K., Munzer, U., & Gudmundsson, A. (2006). The use of remote-sensing data for mass-balance studies at Myrdalsjokull ice cap , Iceland. *Journal of Glaciology 52*(179), 565–573.

Japan Space Syatems. (2012). G-DEM Project. Retrieved from https://www.jspacesystems.or.jp/ersdac/GDEM/E/index.html

Jo, T., & Schmeits, W. H. K. M. (1998). Modelling the response of glaciers to climate warming. *Climate Dynamics* 267–274.

Kargel, J. S., Abrams, M. J., Bishop, M. P., Bush, A., Hamilton, G., Jiskoot, H., … Wessels, R. (2005). Multispectral imaging contributions to global land ice measurements from space. *Remote Sensing of Environment 99*, 187–219. doi:10.1016/j.rse.2005.07.004

Khadka, D., Babel, M. S., Shrestha, S., & Tripathi, N. K. (2014). Climate change impact on glacier and snow melt and runoff in Tamakoshi basin in the Hindu Kush Himalayan (HKH) region. *JOURNAL OF HYDROLOGY*, *511*, 49–60. doi:10.1016/j.jhydrol.2014.01.005

Koing, M., Winther, J.-G., Knudsen, N. T., & Guneriussen, T. (2000). Equilibrium- and firn-line detection with multi-polarization sar – first results. In *EARSeL-SIG-Workshop Land Ice and Snow* (pp. 273–280). Dresden.

Konig, M., Winther, J., & Isaksson, E. (2001). Measuring snow and glacier ice properties from satellite. *Reviews of Geophysics*, *39*(1), 1–27.

Kulkarni, A. V., Dhar, S., Rathore, B. P., & Kalia, R. (2006). Recession of Samundra Tapu Glacier , Chadra River Basin , Himachal Pradesh. *Indian Society of Remote Sensing*, 1–10.

Kulkarni, A. V. (2007). Effect of global warming on the Himalayan cryosphere. *Jalvigyan Sameekhsha*, *22*, 93–108.

Kulkarni, A. V, Bahuguna, I. M., Rathore, B. P., Singh, S. K., Randhawa, S. S., Sood, R. K., & Dhar, S. (2007). Glacial retreat in Himalaya using Indian remote sensing satellite data. *Current Science*, *92*, 69–74.

Kumar, V., Venkataramana, G., & Høgda, K. a. (2011). Glacier surface velocity estimation using SAR interferometry technique applying ascending and descending passes in Himalayas. *International Journal of Applied Earth Observation and Geoinformation*, *13*(4), 545–551. doi:10.1016/j.jag.2011.02.004

Lee, J., Grunes, M. R., Ainsworth, T. L., Du, L., Schuler, D. L., & Cloude, S. R. (1999). Unsupervised classification using polarimetric decomposition and the complex Wishart classifier. *IEEE TRANSACTIONS ON GEOSCIENCE AND REMOTE SENSING*, *37*(5), 2249–2258.

Lee, J.-S., & Pottier, E. (2009). Polarimetric Radar Imaging: From Basics to Applications. Boca Raton London Newyork: CRC Press Taylor and Francis Group.

Leprince, S. (2013). Glacier displacement with low SNR — Glaciology — COSI-Corr. Retrieved from http://tecto.gps.caltech.edu/forum/viewtopic.php?pid=426#p426

Leprince, S., Barbot, S., Ayoub, F., & Avouac, J.-P. (2007). Automatic and precise orthorectification , coregistration , and subpixel correlation of satellite images , application to ground deformation measurements. *IEEE TRANSACTIONS ON GEOSCIENCE AND REMOTE SENSING*, *45*(6), 1529–1558.

Li, S., Benson, C., Gens, R., & Lingle, C. (2008). Motion patterns of Nabesna glacier (Alaska) revealed by interferometric SAR techniques. *Remote Sensing of Environment*, *112*(9), 3628–3638. doi:10.1016/j.rse.2008.05.015

Messerli, B., Viviroli, D., Weingartner, R. (2004). Mountains of the world: vulnerable water towers for the 21st century. *Ambio*, pp 29–34.

Muller, K. (2011). *Microwave penetration in polar snow and ice : Implications for GPR and SAR*. *University of Oslo*, Norway.

NASA. (2011). Landsat 7 Handbook. Retrieved from http://landsathandbook.gsfc.nasa.gov/sysper/

Neelmeijer, J. (2012). Dynamics of the Inylchek glacier (Kyrgyzstan) derived from amplitude tracking using TerraSAR-X Data. *Technische Universitat Dresden.*

Owen, L. A., Derbyshire, E., & Fort, M. (1998). In The Quaternary Glacial History of the Himalaya*. Quaternary Proceedings*, (p. pp 91–120). Chichester.

Owen, L. A., Finkel, R. C., Caffee, M. W., & Gualtieri, L. (2002). Timing of multiple late Quaternary glaciations in the Hunza Valley , Karakoram Mountains , northern Pakistan : Defined by cosmogenic radionuclide dating of moraines. *The Geological Society of America*, *114*.

Pandey, A. C., & Nathawat, M. S. (2012). Morphometric control on glacier area changes in the Great Himalayan Range , Jammu and Kashmir, India. *Research Communications*, *102*(8).

Paterson, W.S.B., 1994. Physics of Glaciers. Third Edition. *Butterworth-Heinemann*

Patrington, K. C. (1998). Discrimination of glacier facies using multi-temporal SAR data. *Jouranl of Glaciology*, *44*(146), 42–53.

Pellika, P., & W.G.Rees. (2009). Remote Sensing of Glaciers. *Taylor & Francis*.

Raina, V. K. (2005). Himalayan Glaciers. *MoEF Discussion Paper*.

Reigber, A., & Scheiber, R. (2003). Airborne differential SAR interferometry : First results at L-Band. *IEEE TRANSACTIONS ON GEOSCIENCE AND REMOTE SENSING*, *41*(6), 1516–1520.

Rott, H., & Matzler, C. (1987). Possibilities and limits of synthetic aperture radar for snow and glacier surveying. *Annals of Glaciology*, *9*, 195–199.

SARscape, 2010. User Guide. sarmap.

Scherler, D., Leprince, S., & Strecker, M. (2008). Glacier-surface velocities in alpine terrain from optical satellite imagery—Accuracy improvement and quality assessment. *Remote Sensing of Environment*, *112*(10), 3806–3819. doi:10.1016/j.rse.2008.05.018

Shimoni, M., Borghys, D., Heremans, R., Perneel, C., & Acheroy, M. (2009). Fusion of PolSAR and PolInSAR data for land cover classification. *International Journal of Applied Earth Observation and Geoinformation 11*, 169–180. doi:10.1016/j.jag.2009.01.004

Shukla, a., Arora, M. K., & Gupta, R. P. (2010). Synergistic approach for mapping debris-covered glaciers using optical–thermal remote sensing data with inputs from geomorphometric parameters. *Remote Sensing of Environment*, *114*(7), 1378–1387. doi:10.1016/j.rse.2010.01.015

Siegert, M.J., 2008. Chapter 6 Numerical modelling of the Antarctic ice sheet, in : Fabio, F., Martin, S. (Eds.), *Developments in Earth and Environmental Sciences*. Elsevier, pp. 235-256.

Small, D., Wemer, C., & Nuesch, D. (1993). Baseline modelling for ERS-1 SAR interferometry. *Geoscience and Remote Sensing Symposium*, 1993. *IGARSS 93*, *1203*(1), 1204–1206.

Strozzi, T., Luckman, A., Murray, T., Wegmüller, U., & Werner, C. L. (2002). Glacier motion estimation using SAR offset-tracking procedures. *IEEE TRANSACTIONS ON GEOSCIENCE AND REMOTE SENSING 40*(11), 2384–2391.

Tiwari, R. K., Gupta, R. P., Gens, R., & Prakash, A. (2012). Use of optical, thermal and microwave imagery for debris characterization in Bara-Shigri glacier, Himalayas, India. *IEEE*, 4422–4425.

Torres, L., Cavalcante, T., & Frery, A. C. (2012). Speckle reduction using stochastic distances. Retrieved from http://arxiv.org/abs/1207.0704

Trouvé, E., Vasile, G., Gay, M., Bombrun, L., Member, S., Grussenmeyer, P., … Koehl, M. (2007). Combining airborne photographs and spaceborne SAR data to monitor temperate glaciers : Potentials and limits. *IEEE TRANSACTIONS ON GEOSCIENCE AND REMOTE SENSING 45*(4), 905–924.

Tso, B. &, & Mather, P. (2009). Classification Methods for Remotely Sensed Data. (Second Edi.). *Taylor & Francis.*

U S Geological Survey. (2014). Landsat 8. Retrieved from http://landsat.usgs.gov/landsat8.php

UNEP. (2009). Recent trends in melting glaciers , tropospheric temperatures over the Himalayas and summer monsoon rainfall over India.

Wagnon, P., Linda, A., Arnaud, Y., Kumar, R., Sharma, P., Vincent, C., … Chevallier, P. (2007). Four years of mass balance on Chhota Shigri glacier , Himachal Pradesh , India , a new benchmark glacier in the western Himalaya. *Journal of Glaciology 53*(183), 603–611.

Water on Earth. (pp. 1–22).

Wilfried Haeberli. *Global glacier changes : facts and figures contents*.

WWF. (2005). An overview of glaciers , glacier retreat , and subsequent impacts in Nepal , India and China.

Zemp, M., & Wilfried Haeberli. (n.d.). *Glaciers and ice caps*. *UNEP*.

Zongli, J., Shiyin, L., Sichun, L., & Xin, W. (2012). Estimate Yengisogat glacier surface flow velocities using ALOS PALSAR data feature-tracking, Karakoram, China. *Procedia Environmental Sciences*, *12*(2006), 646–652. doi:10.1016/j.proenv.2012.01.330

APPENDIX

Appendix: Datasets used in this study

A1: SAR data sets used in this study

Serial No.	Satellite	Band	Date	Polarization	Resolution (m)
1	ERS-1	C	28/03/1996	VV	25
2	ERS-1	C	02/05/1996	VV	25
3	ERS-2	C	29/03/1996	VV	25
4	ERS-2	C	03/05/1996	VV	25
5	ALOS/PALSAR	L	06/04/2009	HH, HV, VH, VV	25
6	ALOS/PALSAR	L	12/04/2011	HH, HV, VH, VV	25
7	ALOS/PALSAR	L	13/09/2009	HH, HV	15
8	ALOS/PALSAR	L	01/08/2010	HH, HV	15
9	RISAT-1	C	05/01/2013	HH, HV	18
10	RISAT-1	C	15/04/2013	HH, HV	18
11	RISAT-1	C	18/08/2013	HH, HV	18
12	RISAT-1	C	01/12/2013	HH, HV	18
13	TanDEM-X	X	25/08/2013	HH	5
14	TanDEM-X	X	28/09/2013	HH	5
15	RADARSAT-2	C	27/01/2014	HH, HV, VH, VV	10

A2: Optical data sets used in this study

Serial No.	Satellite	Sensor	Band	Date	Resolution (m)
1	Lansat-7	ETM	PAN	09/07/1999	15
2	Lansat-7	ETM	PAN	28/08/2000	15
3	Lansat-7	ETM	PAN	28/06/2001	15
4	Lansat-7	ETM	PAN	02/08/2002	15
5	Landsat-8	OLI/TIRS	PAN	23/07/2013	15
6	Landsat-8	OLI/TIRS	PAN	11/08/2014	15
7	Terra	ASTER	VNIR	08/09/2004	15
8	Terra	ASTER	VNIR	30/09/2006	15

Appendix: Confusion matrices using SVM classification

A3: Confusion matrix for SVM classification of ALOS/PALSAR 06/04/2009 datasets.

Class	PZ	IW	GIZ	DS	Debris	Total
PZ	256	8	1	0	4	269
IW	12	152	0	0	1	165
GIZ	0	0	98	1	2	101
DS	0	0	2	146	4	152
Debris	5	3	5	10	84	107
Total	273	163	106	157	95	794

Overall Accuracy = (736/794) 92.6952%

Kappa Coefficient = 0.9051

A4: Confusion matrix for SVM classification of ALOS/PALSAR 12/04/2011 datasets.

Class	PZ	IW	GIZ	DS	Debris	Total
PZ	178	3	0	0	4	185
IW	0	65	0	0	0	65
GIZ	0	0	143	2	0	145
DS	0	0	7	60	1	68
Debris	8	1	2	2	84	97
Total	186	69	152	64	89	560

Overall Accuracy = (736/794) 92.6952%

Kappa Coefficient = 0.9051

A5: Confusion matrix for SVM classification of RISAT-1 multi-temporal datasets.

Class	PZ	GIZ	Debris	Total
PZ	705	28	11	744
GIZ	9	508	13	530
Debris	20	0	412	432
Total	734	536	436	1706

Overall Accuracy = (1625/1706) 95.2521%

Kappa Coefficient = 0.9270